Università degli Studi
di Palermo

Controllo della sintesi e caratterizzazione di nanocompositi di oro e cobalto

Tesi di Dottorato della
Dott.ssa Luisa Sciortino

Tutor
Prof. Antonino Martorana

Co-Tutor
Dr. Alessandro Longo

Coordinatore
Prof. Michelangelo Gruttadauria

Dottorato di Ricerca in Scienze Chimiche
Ciclo xxiii
CHIM/03

Università degli Studi
di Palermo

Control of the synthesis and characterization of gold and cobalt nanocomposites

Ph.D. thesis of
Luisa Sciortino

Supervisor
Prof. Antonino Martorana

Co-supervisor
Dr. Alessandro Longo

Coordinator
Prof. Michelangelo Gruttadauria

Dottorato di Ricerca in Scienze Chimiche
Ciclo xxiii
CHIM/03

Sommario

Sebbene diversi metodi di sintesi siano riportati in letteratura il controllo della struttura, delle dimensioni e della morfologia di nanoparticelle e di nanocompositi è tuttora oggetto di indagine e di studio. L'oro e il cobalto sono tra gli elementi metallici piu' studiati per la grande varieta' di applicazioni in campo tecnologico delle loro nanoparticelle e dei loro nanocompositi. Allo stato metallico e quando raggiungono dimensioni nell'ordine dei nanometri mostrano proprietà molto diverse; l'oro e' chimicamente molto stabile, mentre il cobalto si ossida molto facilmente, inoltre l'oro si impacchetta secondo sequenze di piani cubici, al contrario il cobalto mostra la coesistenza di sequenze esagonali e cubiche con un alto grado di disordine. Anche magneticamente mostrano un comportamento sensibilmente diverso; nella fase bulk il cobalto è l'elemento ferromagnetico che mostra la Temperatura di Curie più alta, ovvero, tra gli elementi della tavola periodica, perde la magnetizzazione residua alla temperature più alta. Quando raggiunge dimensioni nanometriche appare il superpamagnetismo. Al contrario l'oro è totalmente diamagnetico in fase bulk mentre mostra un comportamento ferromagnetico in presenza di particolari agenti di capping e a dimensioni molto ridotte (5 nm). In questo lavoro di tesi, utilizzando diversi protocolli di sintesi e agenti protettivi, è stato studiato il controllo della sintesi in termini di coalescenza e ossidazione di nanoparticelle libere e supportate su wafer di silicio. I campioni, costituiti da nanoparticelle di oro e cobalto, sono stati preparati mediante decomposizione termica e SMAD (Solvated Metal Atom Dispersion). Gran parte dello studio delle proprietà strutturali e morfologiche dei campioni è stato condotto mediante AFM (Atomic Force Microscopy) e con tecniche di luce di sincrotrone: EXAFS (Extended X-ray Absorption Fine Structure), XRD (X-Ray Diffraction), e GISAXS (Grazing Incidence Small Angle X-ray Scattering). La tesi si articola in otto capitoli:

- Capitolo 1: contiene un'introduzione al mondo nanometrico con particolare attenzione alle nanoparticelle ed ai nanocompositi di oro e cobalto;
- Capitolo 2: sono presentate le metodiche sintetiche implementate per la preparazione dei campioni di oro e cobalto;
- Capitolo 3: l'analisi dei dati XAFS ((X-ray Absorption spectroscopy), registrati presso le linee BM08 e BM26 di ESRF (European Synchrotron Radiation Facilities). Gli spettri dei campioni costituiti da nanoparticelle libere

sono stati misurati in trasmissione, mentre gli spettri dei nanocompositi metallo/silicio sono stati registrati in fluorescenza.

- Capitolo 4: il modello matematico, sviluppato per il fitting dei dati HRXRD (High Resolution X-ray Diffraction) acquisiti presso la linea ID31 di ESRF, è descritto. Il capitolo contiene, inoltre, i risutati dell'analisi strutturale (ottenuta con il modello descritto) delle nanoparticelle di cobalto libere;

- Capitolo 5: è riportato lo studio morfologico mediante l'analisi dei dati AFM delle nanoparticelle di oro e di cobalto supportate su silicio. L'influenza degli agenti di capping e l'effetto dovuto alla natura dell'ossido di silicio sono stati approfonditi;

- Capitolo 6: i principi della tecnica GISAXS e i risultati dell'analisi sui campioni di oro su silicio sono descritti;

- Capitolo 7: contiene una discussione dei risultati ottenuti;

- Capitolo 8: le conclusioni generali di tutto il lavoro di tesi sono delineate.

Contents

List of Figures

List of Tables

Chapter 1

Introduction

1.1 Why nanoworld?

A nanomaterial is characterized by the presence in the formulation of structural units having at least one dimension in the nanometer range, usually beteween 1 and 100 nm. At very small particle size it is not unusual that the atomic arrangement is different from the bulk, and that a close dependence of the nanophase properties on particle size, structure and various environmental factor such as supporting materials, embedding matrices or coating materials can be observed. Among the factors that determine the peculiar properties of nanomaterials can be cited [1]:

- surface effects: atoms at surfaces have fewer neighbours than atoms in the bulk. Because of this lower coordination and unsaturated bonds, surface atoms are less stabilised than bulk atoms. The surface-to-volume ratio scales with the inverse size, and therefore numerous properties, such as melting and other phase transition temperatures [2][3], obey the same scaling law.

- quantum size effects: in metals and semiconductors the electron wave functions of conduction electrons are delocalised over the entire particle. Electrons can therefore be described as "particles in a box", and the density of states and the energies of the particles depend crucially on the size of the box. The confinement of electrons to smaller regions gives rise to original size-dependent properties. Ionisation potentials and electron affinities are tuned between the atomic values and the work function of the bulk material by variation of the cluster size. These same properties relate to the availability of electrons for forming bonds or getting involved in redox reactions. Therefore, the catalytic activity and selectivity become dependent on size [4][5].

In the last decades metal nanoparticles have been deeply studied for the peculiar properties

arising from reduced size. The outstanding properties of metal nanoparticles find applications in many different fields, ranging from catalysis, optics, spintronics, medicine [6] and magnetism [7]. There are many examples in literature of metals that change drastically their bulk properties when the nanometer scale is reached. One of the most striking cases is probably represented by gold nanoparticles, that catalyse the water gas shift (WGS) reaction and the oxidation of carbon monoxide at low temperature, in spite of the inert chemical behaviour of the bulk phase [8][9][10][11][12]. Nanocomposite materials constituted of nanosized metal particles embedded in a dielectric matrix have immense technological potential in many fields, such as catalysis, photonics, magnetics, electronics, and single electron devices [13][14]. In order to fabricate nanoscale devices with sought-after properties, the design of novel materials should be necessarily complemented by the ability to control the nanophase synthesis and, for nanocomposites, to deposit and position the nanosized building blocks on suitably designed substrates or matrices [15][16].

In line with the overview given so far, this Ph.D. thesis is concerned with the assessment of protocols allowing an improved control in the synthesis of metal nanoparticles and in the fabrication of metal nanocomposites. The sought control of the synthesis routes necessarily involves a very careful structural characterization, carried out with different and complementary experimental techniques, and some preliminary functional characterization. The preparation of nanomaterials is focussed on two metals, gold and cobalt, that attracted much interest due to the wide variety of applications in the technology of sensors [17][18], catalysts [19][20] and nonvolatile memory devices [21].

1.1.1 Au nanoparticles

Gold is the most studied metallic element in the nanometer range due to high chemical stability and photostability and to fascinating size-related electronic, magnetic and optical properties [22]. Gold nanoparticles find applications in many different fields, for example in catalysis[23], in nanoelectronics [24], and in biomedicine [25]. Traditionally, bulk gold was thought to be chemically inert, but when nanocrystalline gold is dispersed on a support with high surface area its reactivity undergoes a striking enhancement. The size-dependent catalytic activity of Au for the selective oxidation of CO in a hydrogen-rich environment and in the WGS reaction is one of the most remarkable examples of high reactivity of nanoparticles [4], but the use of supported gold nanoparticles in heterogeneous catalysis is reported also for propylene epoxidation, combustion of hydrocarbons, NOx reduction, and hydrogenation reactions. In literature there are several studies on the size and structure [26] of Au nanoclusters and on the effect of an inert or reducible supports (silicon oxide, cerium oxide) on oxidation state and electronic charge distribution [27][28][29][30][11]. Some studies demon-

strated the involvement of gold nanoparticles in biomedical applications, showing that suitable size and shape allow to control the intracellular uptake of proteins, drugs, and oligonucleotides [31] for diagnostic and therapeutic applications. A good deal of papers on nanosized gold concern nanocomposite films, such as Au/Al2O3 [32], Au/ZnO [33], and Au/SiO2 [34]. These nanocomposites have been extensively studied as novel optical materials [35][36], photocatalysts and sensors [14]. Su *et al.* studied multiphoton luminescence of Au nanocrystals prepared by radio frequency co-sputtering technique at glancing angles [37]. Kim reported that the Au nanoparticles in the Au/SiO2 nanocomposite films were aggregated through water treatment [38]. Guczi and co-workers, showed that a correlation exists between the CO oxidation rate and the Au 5d valence band density of states of gold nanoparticles deposited on native-SiO2/Si [19]. However, the authors did not consider explicitly the interactions of gold clusters with the support. Nowadays, this phenomenon is considered as most relevant to explain the striking behaviour of gold in CO oxidation as well as the peculiar electronic structure of nanosized Au.

1.1.2 Co nanoparticles

Among the elements of the *3d* series, cobalt is widely investigated from the point of view of catalytic and magnetic properties. The bulk cobalt structure is *hcp* at room temperature, while a weakly first order transition to the *fcc* arrangement takes place above 477 K with small changes in enthalpy ($\Delta H = 440 kJ/mol$) and volume ($\Delta V/V = 0.0036$) [39]. The two structures differ in the compact sequences of atomic layers: the *hcp* arrangement is characterized by ABAB... sequences, while the *fcc* packing is ABCABC.... Both in bulk and nanosized cobalt the occurrence of stacking faults is often recognized, entailing awkward establishment of structure-properties correlation. A.J.C. Wilson first proposed a mathematical model to elucidate the structural disorder in metallic cobalt [40]. In order to explain the broadening of specific diffraction peaks, he calculated the intensity profiles on the basis of a statistical sequence of stacking faults. In correspondence to the different packing sequences, also bulk anisotropies, as it was studied by Sucksmith and Thompson in 1954 [41], of *hcp* and

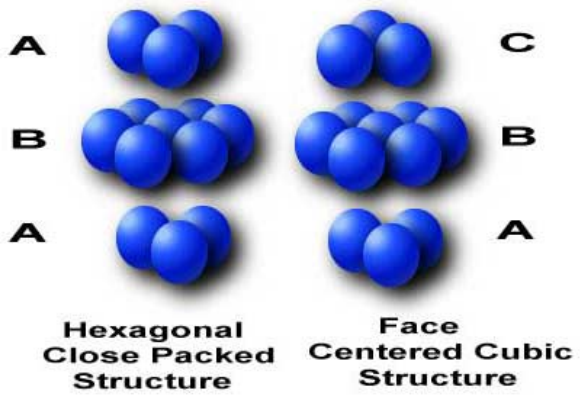

Figure 1.1: *The two stable compact sequences of layers for metal cobalt. Left: the hexagonal close packed structure. Right:the face centered cubic structure.*

fcc Co are rather different, K_{hcp}=$510^6 erg/cm^3$ and $K_{(fcc)}$=$0.810^6 erg/cm^3$, where K are the magnetic anisotropies, giving the dependence of the magnetic properties on the direction. Moreover, the magnetic properties of Co depend strictly on the close packing arrangement, with the *hcp* structure characterized by one easy axis along the [001] plane and the *fcc* arrangement having four easy axes along the $< 111 >$ directions [42]. Also the nanophase magnetic properties are strictly dependent on the atomic arrangement, as it is observed in several papers [43]. In particular, Sort *et al.* demonstrated that the *hcp-fcc* transformation induced by ball milling is ruled by a process of stacking faults accumulation and that the stacking fault probabilities can be correlated with the magnetic properties [43][44]. Although the *hcp* arrangement is the stable bulk Co form at thermodynamic equilibrium, it is widely reported in literature that cobalt nanocrystals and films exhibit a *fcc* structure at room temperature [45]. Due to the relevance of this matter, several research groups investigated by different computational approaches the structure and stability of Co nanoclusters [46][47][48]. It was demonstrated that chemical procedures involving different capping agents allow to obtain *fcc* and/or *hcp* structural arrangements with expected different magnetic properties also for other metals such as nickel [49]. The synthesis methods using different capping agents are widely described in the literature, pointing out that the capping agents:

- stabilize the metal particles towards agglomeration;
- interact with the metal phase after nucleation, allowing to control shape, crystal structure and nanoparticles size [50][51].

So, a good capping agent is able to prevent coalescence and, if necessary, oxidation. In addition, a capping agent could address the structure toward a selected structural arrangement [52]. Then, it is evident the crucial importance of the synthetic procedure to control the growth of metal clusters in order to obtain magnetic material with improved and selected characteristics. In consideration of the close link between crystal structure and magnetic properties, a detailed analysis of the structural disorder of cobalt nanoparticles is also essential to establish reliable correlation with the magnetic properties. Taking into account that the storage systems for the near future are required to display data densities of 1 Tb per square inch and data writing speed of 2Gb per second for [53], synthesis control and accurate structural analysis are essential in view of the development of suitable magnetic materials for the next years' technology.

In summary, gold and cobalt have very different and peculiar properties: gold has high chemical stability, while cobalt is easily oxidized; gold is *fcc* whereas cobalt can be found in the *hcp* or *fcc* arrangements, very often simultaneously present and with a noticeable amount of stacking disorder of atomic layers. From the point of view of magnetic properties, both metals show a

size-dependent behaviour. Bulk cobalt is ferromagnetic, but nanosized metal particles, below approximately 15-20 nm, are superparamagnetic. However, the loss of a stable magnetization in Co nanoparticles can be overcome in suitably tailored environments, as was reported by Nogues *et al.*, who demonstrated that the superparamagnetic behaviour is suppressed in cobalt nanoparticles of 40 Å embedded in an antiferromagnetic CoO matrix [54]. On the other hand, bulk gold is diamagnetic, while in the nanometer range and in presence of a particular capping agent exhibits a different magnetic behaviour: Hori *et al.* observed a superparamagnetic behavior in 30 Å Au nanoparticles embedded in a polymeric matrix at low temperatures [55] while some years later the direct evidence of the ferromagnetism of 19 Å Au nanoparticles was found [56]. Recently, a theoretical study demonstrated that the magnetic behaviour of a gold nanocluster depends sensitively on the nanoparticle shape [57]. Therefore, the nature of the surface of the substrate, and in particular the presence of defects acting as nucleation centers, has a direct consequence on the morphology and can influence the magnetic properties of the deposited gold nanoparticles [58].

In conclusion, the properties of the Co and Au nanomaterials are so peculiar with respect to the bulk phase, that the achievement of a tight control in the preparation could open new perspectives from the point of view of basic knowledge and applications.

1.2 Aims and plan of the dissertation

Although many synthetic routes are reported in literature, the control of size, structure and morphology of nanoparticles and nanocomposites is still object of investigation. The growth control, both of free particles and of particles supported on silicon wafers, and the protection against coalescence and oxidation are investigated in this thesis, by exploiting different preparation protocols and capping agents. Also the closely related investigation of the outcome of the syntheses is considered, with a number of complementary experimental techniques involving EXAFS, XRD, AFM, GISAXS. A preliminary analysis of the magnetic properties of some cobalt samples is accomplished by MFM.

The thesis is organized in seven chapters:

- Chapter 1: the state of the art and the scientific debate concerning the investigated materials is accounted;
- Chapter 2: the preparation of gold and cobalt materials is described. The synthesized samples are constituted of free nanoparticles coated with specific capping agent and of nanoclusters grown on silicon wafers;
- Chapter 3: reports the analysis of the XAFS (X-ray Absorption spectroscopy) data, that were acquired at the BM26 and BM08 beamlines of the ESRF (European Synchrotron Radiation Facilities). Unsupported samples

are investigated in trasmission geometry and Si-supported in fluorescence mode.

- Chapter 4: the mathematical details of the model developed to fit the HRXRD (High Resolution X-ray Diffraction) patterns of cobalt samples, acquired at the ID31 of the ESRF (European Synchrotron Radiation Facilities), are given. The structural analysis results, based on the model, are also reported;

- Chapter 5: the supported samples are analized by Atomic Force Microscopy, obtaining knowledge about morphology, height function distribution, and sample roughness. The influence of the capping agents, of the solvent used and of the native silicon oxide layer is investigated;

- Chapter 6: the GISAXS (Grazing Incidence Small Angle X-ray Scattering) results are described. With the complementary information of EXAFS and AFM, a thorough picture of the investigated materials is obtained;

- Chapter 7: A discussion, concerning the results, is reported;

- Chapter 8: the general conclusions of this study are drawn.

Chapter 2

Experimental procedures

2.1 Methods and materials

The reagents used for the synthesis are: cobalt foil (+99.9% Sigma-Aldrich), gold foil (+99.9% Sigma-Aldrich), dicobalt octacarbonyl (≥ 95% Fluka), trioctylphosphine (≥ 90% Aldrich) [50], trioctylphospine oxide (≥ 98.5% Fluka) [59], octadecylamine (≥ 99% Fluka), trioctylamine (≥ 93% Merck), heptane (≥ 95% Sigma-Aldrich), toluene (≥ 99.5% Sigma-Aldrich), mesitilene (≥ 98% Sigma-Aldrich), acetone(≥ 98% Sigma-Aldrich). These reagents were used as received, without any pretreatment. Some molecules are labelled as follow:

- TOP for trioctylphosphine
- TOPO for trioctylphosphine oxide
- ODA for octadecylamine
- TOA for trioctylamine

Metal nanoparticles were synthetized by two different routes: Thermal Decomposition (TD) [60] and Solvated Metal Atom Dispersion (SMAD) [61]. The two techniques are antithetical, as the TD route is a bottom-up, while the SMAD is a top-down method. Thermal decomposition is carried out putting a metal precursor, often in the valence state 0, and a capping agent in an organic solvent with high boiling point and heating under argon flux. The SMAD technique involves the vaporization of the bulk metal in low pressure argon atmosphere (10-200 mTorr) and then the addition of a capping agent solution. In both routes, the inert atmosphere is necessary to prevent the oxidation of the metal nanoclusters, especially in the case of cobalt. The TD route was used to synthesize Co free nanoparticles, while supported Au and Co samples were prepared by SMAD. The Au and Co nanoparticles were supported onto silicon wafers bearing a native oxide layer spontaneously grows up on the silicon surface. The capping agents used in the TD and SMAD routes to prevent the oxidation and the coalescence of

the metal nanoparticles are organic molecules like amines and alchilic phosphines

2.2 Thermal decomposition

The TD syntheses were carried out using the dicobalt octacarbonyl as precursor of metal cobalt; the following steps are involved[60]:

- $1.4 * 10^{-3} mol$ (0.5 g) of $Co_2(CO)_8$ and the capping agent are put into 25 mL of the organic solvent at boiling temperature under continuous argon flow;
- the solution is kept for about 3 hours under reflux;
- the samples are dried under vacuum, so obtaining the powder samples.

With the TD route I prepared two sets of samples. For the sample set 1 the used organic solvent are toluene (b.p. 393K) and mesytilene (b.p. 438K). Trioctylphosphine, trioctylphospine oxide, and octadecylamine were used as capping agent. Samples not containing capping agent were also prepared as reference. The scheme of synthetic condition for set 1 is reported in table 2.1

For the sample set 2 the used organic solvent are heptane (b.p.371K) toluene (b.p.393K), mesytilene (b.p.438K). Troctylamine and octadecylamine were used as capping agent. The conditions of preparations of these samples are reported in table 2.2. The morphology and the size of the nanoparticles were determined by TEM (Transmission Electron Microscopy) measurement carried out at the IMM-CNR of Bologna. The TEM images are shown in appendix A and witness the presence of nanoparticles of 2-6 nm diameter.

Table 2.1: *Synthetic parameter for the set 1 of sample prepared by TD route with a 100:1 ratio between metal atoms and capping agents.*

	Toluene	**Mesytilene**
no capping	a1	a2
TOP	b1	b2
TOPO	c1	c2
ODA	d1	d2

2.3 SMAD

The SMAD preparation route is carried out in a glass reactor linked to a vacuum pump. The metal foil is put in a sampleholder constituted of a cone rolled tungsten wire covered by alluminium oxide, shown in fig.2.1. The metal vaporization is obtained by an electric current flowing through the sample holder. For standard SMAD synthesis[62], typical working parameters to obtain a macroscopic quantity (about 150mg) of cobalt nanoparticles, are a vaporization time of about 30 min and an applied potential difference of 7 V. The technique involves the deposition of an organic solvent (e.g. toluene) on the walls of the metal vapour reactor cooled at 77 K (liquid-nitrogen temperature) [61] . The metal atoms are

Table 2.2: *Synthetic parameters for the set 2 of samples prepared by TD route with different ratios between metallic atoms and capping agents.*

Sample name	**solvent**	**capping**	**Co/capping**	**volum** ($[mL$)
D3	heptane	ODA	80	50
D4	heptane	ODA	500	50
D15	mesytilene	ODA	200	50

Figure 2.1: *The sampleholder in the SMAD apparatus is constituted of a cone rolled tungsten wire, that is linked to two electrods, covered by an aluminium oxide.*

vaporized under controlled atmosphere and subjected to a rapid trapping in the frozen solvent matrix on the walls. Then, the capping agent solution (10 mL) is injected in the reactor and the temperature is raised to RT.

2.3.1 Tuning of metal amount

Although the classic SMAD technique is widely described and applied in literature [63] [11], to my knowledge this route was never used to support metal nanoparticles onto a silicon wafer. Hence, to tune the amount of deposited metal in order to obtain a thin film of deposited nanoparticle, preliminary study was carried out. The deposition of the optimal metal amount per support unit area was achieved by a fine tuning of vaporization times on different silicon slabs of known area. The supported metal amount was determined by ICP-MS (Inductively Coupled Plasma Mass Spectroscopy); experiments on the solutions obtained by treatment of the Co/Si samples with nitric acid and of the Au/Si samples by the *aqua regia* solution, table 2.4 reports the respective metal amount per unit area.

The results reported in table 2.4 can be compared with the number of atoms needed to obtain a cobalt or gold atomic monolayer, shown in table 2.3. In order to promote the growth of a monolayer, the smaller vaporization times reported in table 2.4 were chosen. It is worth to notice that

Table 2.3: *Number of metal atoms per monolayer.*

	Atomic radius (pm)	atoms number/cm^2 per monolayer
Au	179	9.94 E+14
Co	152	1.38 E+17

the increase of the amount of deposited metal is not consistent with the increase of the vaporization time. In other words, for a vaporization time equal to 600 s it would be expected a metal mass twice larger than the vaporized metal obtained with a vaporization time equal to 300 s; probably this effect is due to a dead time during which the vaporization is not yet started.

2.3.2 Si-supported samples

Gold nanoclusters were deposited on native-SiO_2/Si by the SMAD technique to assure an effective deposition of the metal vapor on the surface, the crucible containing the gold foil was located at about three centimetres from the silicon slab; the solvent pressure inside the reactor limits the sintering of the cluster during the deposition step. The value of applied voltage and the evaporation time also allow to control the particle size: in particular, the rate of metal particle growth depends on the former parameter, whereas the latter rules the overall metal amount. The deposition of gold clusters was performed for all samples applying a potential of about 7 V for 180 s at a pressure of 150 mTorr. For the preparations of the gold nanocomposites the selected conditions are summarized as follow:

- introduction of the solvent ($\approx 1mL$) in reactor cooled at 77 K (liquid-nitrogen temperature);
- vaporization for 180 s of the gold foil on the silicon wafer at 150 mTorr under Argon atmosphere;
- injection of the solvent ($2mL$) in the reactor;
- warming to room temperature.

Table 2.4: *Metal amount per area unit determined by ICP measurements.*

Metal	Vaporization time (s)	mg/cm^2	atoms/cm^2
Au	180	0.022	6.50 E+16
Au	300	0.172	5.26 E+17
Co	300	0.061	6.30 E+17
Co	600	0.226	2.31 E+18

As reported in table 2.5, Au was vaporized on four silicon wafer substrates. Three substrates, different for dopant type and dopant concentration (see table 2.5) were used and the corresponding samples were labelled, respectively, as Au1, Au2, and Au3. The fourth sample, Au4, was subjected to a thermal treatment before the metal deposition in order to obtain a thick layer ($591nm$) of silicon oxide. The thickness of native oxide formed on the surface of silicon after several days

Table 2.5: *Synthetic conditions of the Au/Si nanostructured samples*

Sample name	type of support	resistivity Ωcm	oxide	solvent	doping (cm^{-3})
Au1	p-type	0.8-1.1	native	acetone	1.62
Au2	p-type	0.5-1.0	native	acetone	2.3
Au3	n-type	0.07-1.0	native	acetone	7.14
Au4	p-type	2.0-10	thermal	acetone	0

in air could vary from 5 to 20 Å depending on preparation conditions [64]. In our case, the native oxide thickness was about of 1 nm with a roughness of about 0.5 nm, for all the samples.

The deposition of cobalt was carried out on native-SiO_2/Si wafers, setting a potential of about 7 V, a pressure of 30 $mTorr$ and an evaporation time of 300 s. The main steps for the preparations of the cobalt nanocomposites are summarized here:

- introduction of the solvent ($\approx 1mL$) in reactor cooled at 77 K (liquid-nitrogen temperature);
- vaporization for 300 s of the cobalt foil on the silicon wafer at 30 mTorr under argon atmosphere;
- injection of the capping agent solution ($2mL$) in the reactor;
- warming to room temperature.

As reported in table 2.6 Co was vaporized on silicon wafer in presence of three different solvent that are mesytilene, toluene, and heptane. Two samples were prepared in presence of ODA as capping agent.

Table 2.6: *Synthetic conditions of the Co/Si nanostructured samples*

Sample name	ODA (mg)	Solvent
Co-mes	-	mesytilene
Co-mes-ODA	8.2	mesytilene
Co-tol	-	toluen
Co-tol-ODA	8.1	toluen
Co-ept	-	heptane

Chapter 3

XAFS

3.1 XAFS equation: a simple model

XAFS (X-ray Absorption Fine Structure) spectroscopy is a versatile tool to investigate systems at the atomic and molecular scale. It can be applied to any sample, regardless of the long-range order, because the technique is sensitive to the local environment of a specific chemical element. The basic physical quantity that is measured in a XAFS experiment is the x-ray absorption coefficient $\mu(E)$ as a function of the incoming x-ray energy E. When an incident x-ray beam passes through the matter, the intensity of the transmitted beam follows the Lambert-Beer's law

$$I = I_0 e^{-\mu t} \tag{3.1}$$

where I_0 is the intensity of the incident beam, I is the intensity of the transmitted beam, t is the thickness of the sample, and μ is the linear absorption coefficient [65]. For isolated atoms, the coefficient $\mu(E)$ increases as Z^4, and decreases approximately as $\frac{1}{E^3}$ [66], where E is the energy of the incoming beam. The above outlined general behaviour is modified at specific x-ray absorption edges, that are characteristic of the atomic species present in the sample and correspond to the ejection of a photoelectron (1s for the K edge, 2s for the L1 edge, 2p for the L2 and L3 edges). The XAFS spectrum is divided in two distinct portions: the XANES (X-ray Absorption Near-Edge Structure) region, typically within $50eV$ from the main absorption edge, and the EXAFS (Extended X-ray Absorption Fine Structure). The XAFS spectroscopy requires an x-ray beam of finely tunable energy and with high flux and brilliance, therefore all modern XAFS experiments are performed at Synchrotron Radiation Sources

3.1.1 EXAFS

The EXAFS refers to the oscillatory variation of the x-ray absorption as a function of photon energy beyond the edge [65]. The ejected elec-

tron could be represented as a spherical wave that is originated at the absorber and backscattered by the neighbouring atoms (fig.3.1). The interference between the outgoing and backscattered photoelectron waves, that is a function of the interatomic distances and of the photoelectron wavelength λ, gives rise to the oscillations of the x-ray absorption coefficient μ. To obtain the sought structural information, the EXAFS function $\chi(E)$ is defined as follow:

$$\chi(E) = \frac{\mu(E) - \mu_0(E)}{\mu_0(E)} \tag{3.2}$$

where $\mu(E)$ is the measured x-ray absorption coefficient and $\mu_0(E)$ is the atomic x-ray absorption coefficient. The EXAFS function is usually expressed as a function of the photoelectron wave vector k, through the well-known relation between k and E:

$$k = \sqrt{\frac{2m(E - E_0)}{\hbar^2}} \tag{3.3}$$

where m is the mass of the electron and E_0 is the edge energy. The experimental EXAFS signal $\chi(k)$ is then analysed by the theoretical *EXAFS function*

$$\chi(k) = \sum_j \frac{N_j S_0^2 f_j(k) e^{-2\sigma_j^2 k^2}}{kR_j^2} e^{-\frac{2R_j}{\lambda_j(k)}} \sin[2kR_j + \delta_j(k)] \tag{3.4}$$

where j is referred to the $j-th$ coordination shell, N_j is the coordination number, R_j is the average distance to the neighbouring atoms, $f_j(k)$ is the backscattering amplitude, the term $e^{-2\sigma_j^2 k^2}$ is the Debye-Waller factor, $\delta_j(k)$ is the total phase shift, $\lambda_j(k)$ is the electron mean free path and S_0^2 is the amplitude reduction factor.

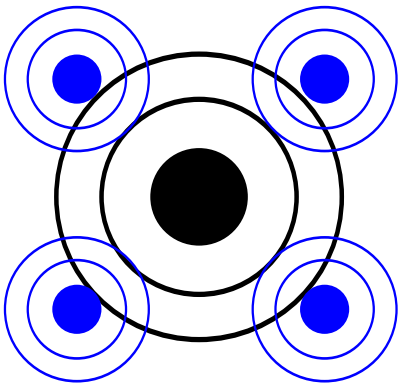

Figure 3.1: *Scheme of the interference between incoming and backscattered photoelectron waves: in black the absorber atom, in blue the nearest neighbours.*

3.2 Experimental details

The Co K-edge (7.7 keV) XAFS data were recorded at the ESRF (European Synchrotron Radiation Facility, Grenoble, France) in transmission geometry at the DUBBLE-BM26 beam-line and in fluorescence mode at the GILDA-BM08 beam-line. The Au L3-edge data were recorded in fluorescence mode at the GILDA-BM08 beam-line. The storage ring operates at 2.4 GeV and 130 mA. The beam-line DUBBLE was equipped with a Si (111) double crystal monochromator with energy resolution $2 * 10^{-4}$, while GILDA was operated with Si (311) crystals in dynamical sagittal focusing mode. The measurements in transmission mode were performed by using two gas ionization chambers filled with a N_2/Ar mixture at different composition for the inci-

dent I_0 and transmitted I_1 beam, respectively. The samples were crushed by grinding in a mortar, pressed in self-supporting wafers and mounted in a sample holder suitable for EXAFS data collection. The fluorescence data were collected by with a 13-elements high purity Ge detector. For energy calibration, XAFS spectra were also acquired for Co foil and Au foil. All the measurements were performed at liquid-nitrogen temperature (LN) to limit the thermal disorder effects that damp the EXAFS oscillation, thus allowing the collection of high quality data, well above the instrumental noise, in a wide range of photo-electron wave vector magnitude.

The data normalization shown in section 3.3.2 is carried out using the Ifeffit package [67][68]. Both data extraction and EXAFS analysis described in section 3.3.3 are carried out by the GnXAS package [69]. The fitting runs are performed in k-space using a k^3 weighting scheme. The refined parameters for *hcp* and *fcc* structures are the lattice parameters, the Debye–Waller parameters, the angles of the three body interactions, and the nanoparticle size, accounting for the reduction of coordination numbers in small particles according to the equation derived by Borowski [70]

$$N_i = N\left(1 - \frac{3}{4}\frac{r_i}{d} + \frac{1}{16}\left(\frac{r_i}{d}\right)^3\right) \qquad (3.5)$$

where N_i is the coordination number of the i-th shell, N is the ideal coordination number, r_i is the $i{-}th$ shell distance and d is the average radius of the nanoparticle. The coordination numbers are calculated on the basis of the crystal structure of nanoparticles and rescaled by the Borowski's equation (3.5). In the case of the D3 and D4 samples and of some supported samples, that exhibit an oxide phase, the first and the second shell of cobalt oxide are added to the model to obtain a satisfactory fit. The limited number of refined parameters enables a robust fitting and consistent results, since all the interatomic distances are expressed as a function of lattice parameters.

3.3 EXAFS: analysis and discussion

3.3.1 Gold samples analysis

The EXAFS data of gold samples are analysed with the GnXAS package using the approach described in ref. [26], that is briefly accounted below. The local atomic arrangement around the absorbing atom is decomposed into model atomic configurations $\gamma(2)...\gamma(n)$ containing 2, ..., n atoms, respectively. The theoretical EXAFS signal $\chi(k)$, where k is the modulus of the photo-electron wave vector, is given by the sum of the n-body contributions, which are calculated considering the effects of all the single and multiple scattering (MS) paths between the n-atoms. In the structural analysis of the Au^0 environment, only six parameters are needed: the lattice constant (from which the next-neighbour distances depend), the Debye–Waller parameters, the two angles of 120° and 180° of the three-body configuration and the nanoparticle size. The results are summarized in table 3.1 and the fittings, obtained assuming an *fcc* arrangement of Au atoms, are reported in figs.3.2, 3.3, 3.4 and 3.5.

3.3.2 Qualitative analysis of the cobalt samples

XAFS data of the samples of set 1, prepared using thermal decomposition (table 2.1), were collected on the cobalt K-edge in order to study the oxidation state of the cobalt nanoparticles as a function of the solvent and of the capping agent. In fig.3.6, the normalized absorption coefficients and the XANES spectra are

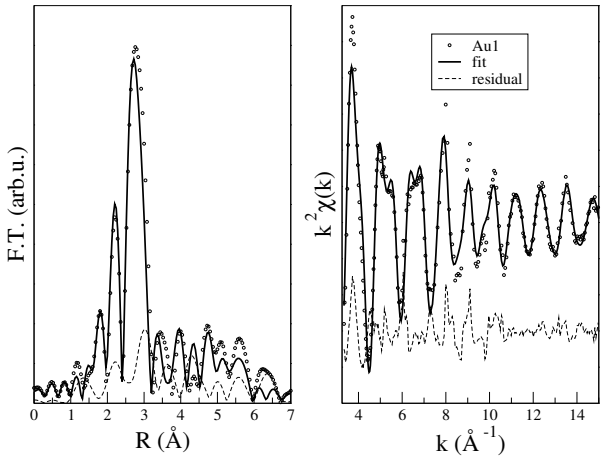

Figure 3.2: *Fit of the EXAFS spectrum of the Au1 sample performed in k-space. Left panel: Fourier transform magnitude of the experimental and fitted signal. Right panel: Calculated EXAFS spectrum generated on the basis of cubic arrangements. The experimental data and the fitting residual are also shown.*

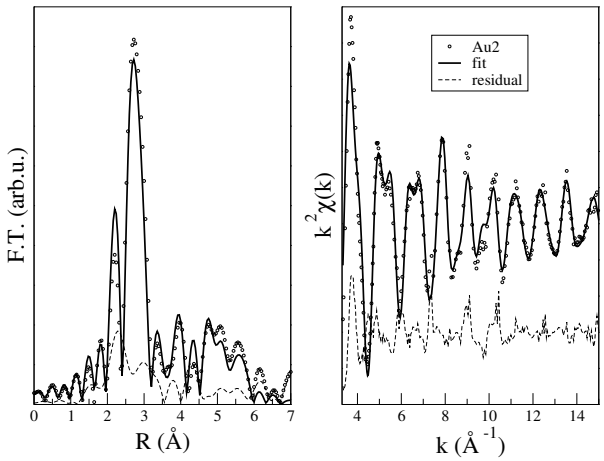

Figure 3.3: *Fit of the EXAFS spectrum of the Au2 sample performed in k-space. Left panel: Fourier transform magnitude of the experimental and fitted signal. Right panel: Calculated EXAFS spectrum generated on the basis of cubic arrangements. The experimental data and the fitting residual are also shown.*

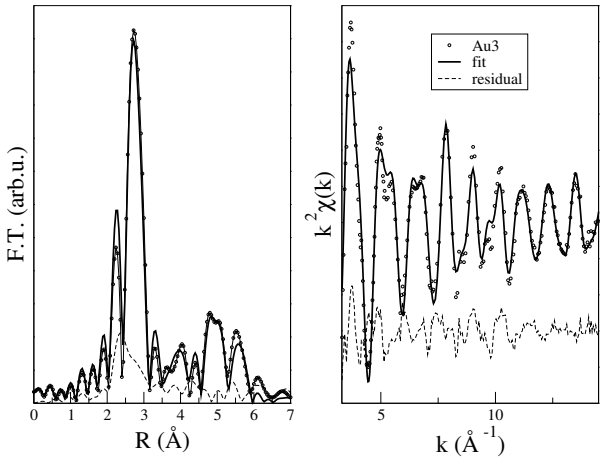

Figure 3.4: *Fit of the EXAFS spectrum of the Au3 sample performed in k-space. Left panel: Fourier transform magnitude of the experimental and fitted signal. Right panel: Calculated EXAFS spectrum generated on the basis of cubic arrangements. The experimental data and the fitting residual are also shown.*

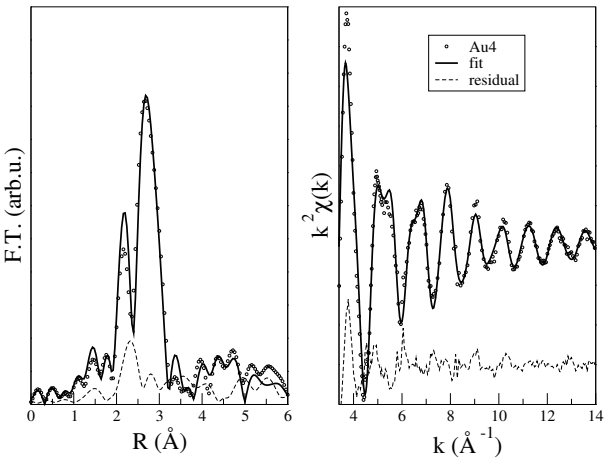

Figure 3.5: *Fit of the EXAFS spectrum of the Au4 sample performed in k-space. Left panel: Fourier transform magnitude of the experimental and fitted signal. Right panel: Calculated EXAFS spectrum generated on the basis of cubic arrangements. The experimental data and the fitting residual are also shown.*

Table 3.1: *EXAFS results for Au samples. R_i, σ_i and R_c are respectively the radii of the i-th shell, the Debye-Waller parameters of the i-th shell and the nanoparticle radius. According to the fcc arrangement, the radius of the first shell is calculated as a function of the lattice parameter R_2, whereas the radii of the III and IV shell are calculated as a function of the θ_1 and θ_2 angles respectively. The errors are on the last digit. The reference Au values are reported in the last column.*

	Au1	Au2	Au3	Au4	Ref.
R_1 (Å)	2.86	2.86	2.864	2.85	2.880
σ_1 (Å^2)	0.0038	0.0034	0.0032	0.0060	-
R_2 (Å)	4.05	4.04	4.05	4.03	4.07
σ_2 (Å^2)	0.0073	0.0048	0.0049	0.0190	-
θ_1 (°)	121	120	121	120	120
θ_2 (°)	179.8	180.1	179.8	180.0	180
R_c (Å)	16.5	16.8	17.0	11.8	-

shown. The samples synthesized using toluene as solvent are drawn using red lines, while those prepared with mesytilene are reported in blue. Cobalt foil and cobalt oxide are also shown as reference. The samples are characterized by smaller oscillations with respect to the reference cobalt foil and cobalt oxide, due to the nanometer size of the samples. From a qualitative point of view, it is possible to observe in the pre-edge region of each spectrum, except for CoO, the presence of a shoulder (fig.3.6) that is a fingerprint of the cobalt in zero valence state; in fact, this feature is very evident in the cobalt foil. The samples a1, b1, c1 and d1, that were prepared with toluene, are characterized by a pronounced white line close in energy to the white line of the oxide reference sample. In the samples synthesized with mesytilene this feature is much less evident.

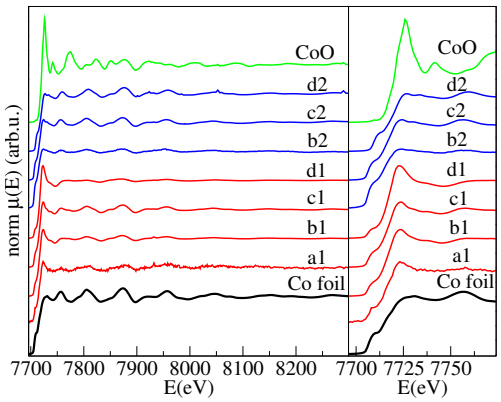

Figure 3.6: *Normalized x-ray absorption coefficients, left panel, and XANES, right panel, for the sample set 1 (table 2.1) on cobalt K-edge are shown and shifted for sake of clarity. Cobalt foil and Cobalt oxide are shown as reference.*

3.3.3 Cobalt local structure model

The EXAFS data are analyzed with the GnXAS package. In the XRD patterns (reported in chapter 4) the *fcc* and the *hcp* lines are simultaneously present. Then, it seems likely that the model of Co local structure should take into account both arrangements. For the *fcc* sequences, two γ^2 are used to fit the first and second shell, respectively, while three γ^2 are necessary to account for *hcp* arrangement. In the *fcc* structure the first shell distance is linked to the lattice parameter, a_c, by $R_1 = a_c/\sqrt{2}$. The higher shells are calculated according to two three-body η^{31} and η^{32} contributions: the third shell is simulated by an isosceles triangle with two first-neighbour bond sides and a vertex angle $\theta_1 = 120°$, whereas the fourth shell, in which the multiple scattering contributions are particularly strong, is calculated from the degenerate ($\theta_2 = 180°$) triangle constituted of three aligned first neighbours. For the *hcp* arrangement, the first shell distance is linked to the lattice parameter a_h and the

Table 3.2: *Details of the fcc EXAFS components. The III and IV shell signals are calculated as 3-body multiple scattering paths. The sides of the triangular paths are given by first neighbour distances forming the specified angles. The IV shell triangle degenerates into a straight path with enhanced photoelectron focussing effect. Coordination number is labelled as C.N.*

Shell	2-body	Shell length		C.N.
I	γ_1^2	$R_1 = a_c/\sqrt{2}$		12
II	γ_2^2	$R_2 = a_c$		6
	3-body	sides	angle	
III	η_1^3	R_1, R_1	120°	24
IV	η_2^3	R_1, R_1	180°	12

Table 3.3: *Details of the hcp EXAFS components. For the 3-body terms, the sides and the angles of triangular paths are given. Subshell splittings are originated by the symmetry-related independent variation of the hexagonal lattice constants a_h and c_h. Coordination number is labelled as C.N.*

Shell	2-body	Shell length		C.N.
I	γ_{11}^2	$R_{11} = a_h$		6
	γ_{12}^2	$R_{12} = \sqrt{a_h^2/3 + c_h^2/4}$		6
II	γ_2^2	$R_2 = \sqrt{a_h^2 4/3 + c_h^2/4}$		6
III	γ_3^2	$R_3 = c_h$		2
	3-body	sides	angle	
IV	η_{11}^3	R_{12}, R_{12}	120°	6
	η_{12}^3	R_{11}, R_{12}	120°	12
V	η_{21}^3	R_{12}, R_{12}	146°	12
VI	η_3^3	R_{11}, R_{11}	180°	6

second shell distance is linked to the *hcp* lattice parameter, a_h, by $R_{11} = a_h\sqrt{2}$. The small contribution of the distance corresponding to c_h parameter is also taken into account due to the fact that this distance is typical in an *hcp* arrangement and absent in a cubic sequence of layers. The higher shells are calculated using three isosceles triangles with two first-neighbour bond sides and vertex angles $\theta_1 = 120°$, $\theta_2 = 146°$ and $\theta_3 = 180°$ corresponding, respectively, to the η^{31}, η^{32} and η^{33} terms. The three-body configurations η^{31} and η^{32} are described using a first-neighbour distance that is geometrically related to the hexagonal lattice parameters by $R_{12} = \sqrt{a_h^2/3 + c_h^2/4}$. For an ideal compact packing c_h/a_h is equal to 1.633, but in the employed model the a_h and c_h parameter are independent in order to take into account any distortions. The R_{12} distance is defined by the a_h lattice parameter and a proportionality coefficient *ratio*:

$$ratio = \frac{a_h}{R_{12}} \tag{3.6}$$

The configurations for the hexagonal arrangement are sketched from fig.3.10 to 3.13. In summary, only few parameters are needed for both *hcp* and *fcc* arrangements: the lattice constants (from which the next-neighbour distances depend), the Debye–Waller parameters, the angles of the three body configurations and the nanoparticle size, accounting for the reduction of coordination numbers in small particles (eq.3.5).

3.3.4 Cobalt foil analysis

First, the analysis of the cobalt foil spectrum is carried out according to a *hcp* or *fcc* arrangement fixing the coordination numbers at the ideal ones. In fig.3.14 the calculated Fourier transform magnitudes using exclusively the *hcp* or the *fcc* model are reported. As it is evident by inspection, neither the *hcp* nor the *fcc* model allows to fit the EXAFS experimental data, especially the range between 3.5 and 5.0 Å, relative

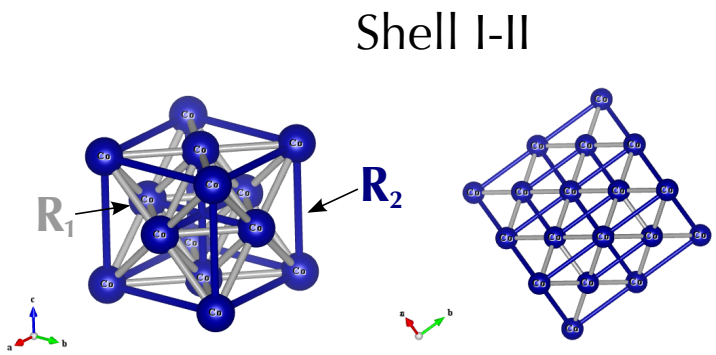

Figure 3.7: *The configurations used for the I and the II shell of the fcc arrangement are sketched. Left panel: the distances are underlined by the arrows. Right panel: The overlapping of the planes is emphasized.*

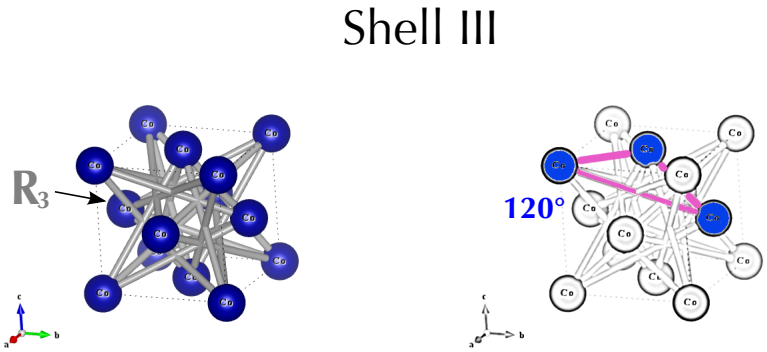

Figure 3.8: *The configuration used for the III shell of the fcc arrangement is sketched. Left panel: the distance is underlined by the arrows. Right panel: The three-body configuration, that involve the* $\theta_1 = 120°$ *is stressed out.*

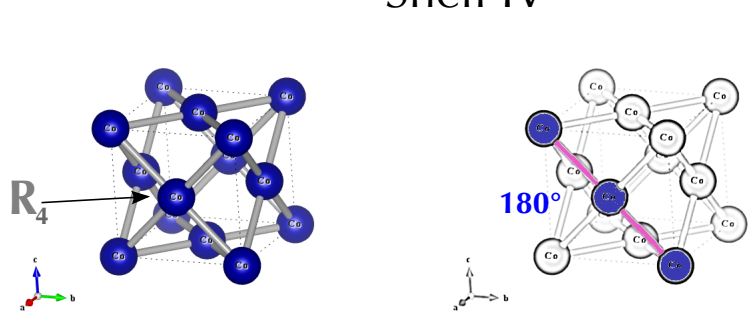

Figure 3.9: *The configuration used for the IV shell of the fcc arrangement is sketched. Left panel: the distance is underlined by the arrows. Right panel: The three-body configuration, that involve the* $\theta_1 = 180°$ *is stressed out.*

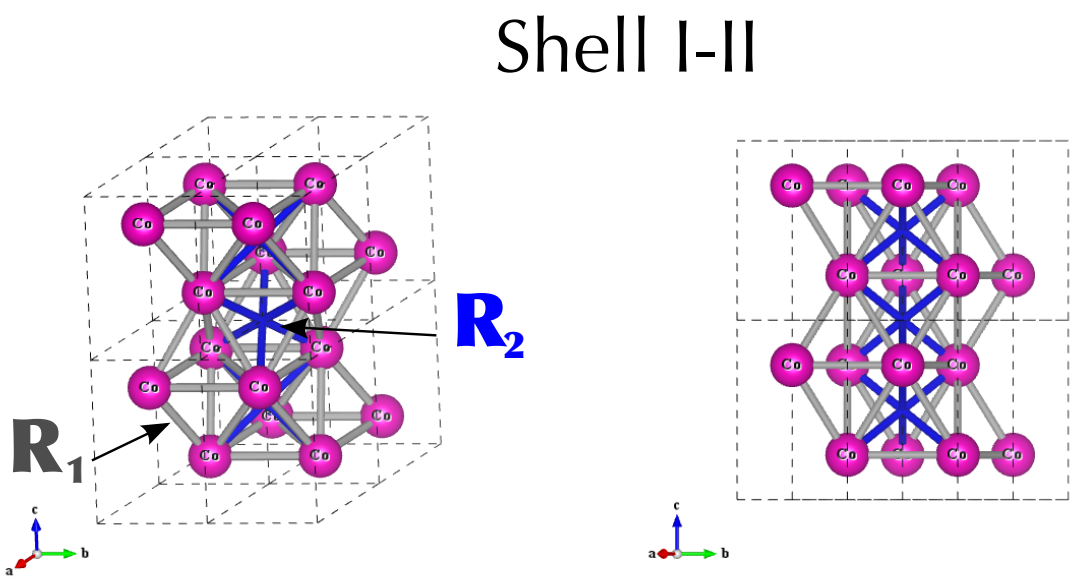

Figure 3.10: *The configurations used for the I and the II shell of the hcp arrangement are sketched. Left panel: the distances are underlined by the arrows. Right panel: The overlapping of the planes is emphasized.*

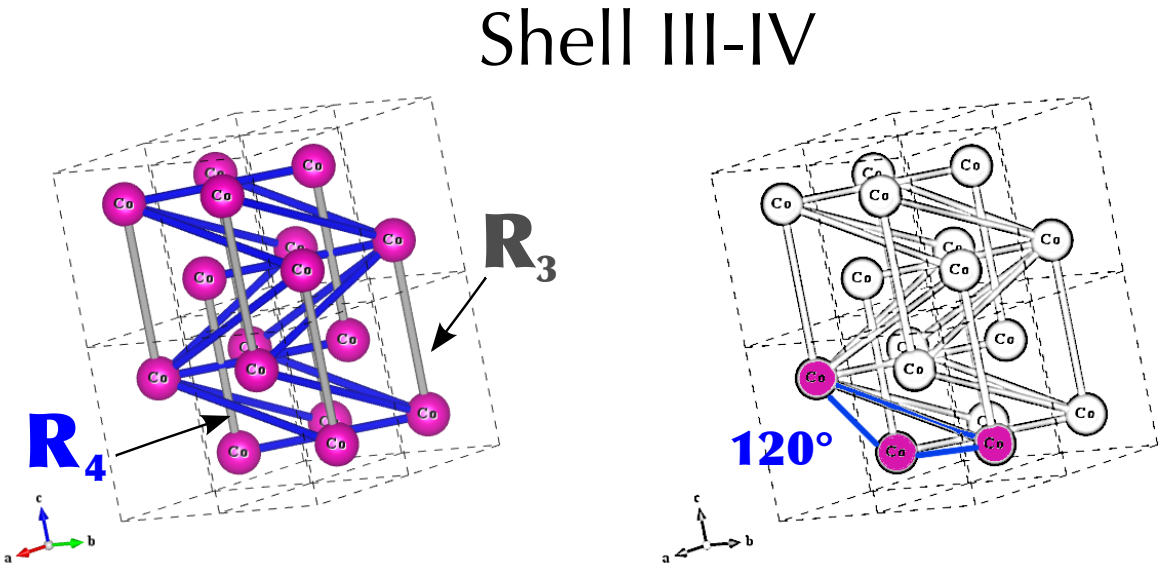

Figure 3.11: *The configurations used for the III and the IV shell of the hcp arrangement are sketched. Left panel: the distances are underlined by the arrows. Right panel: The three-body configuration, that involve the* $\theta_1 = 120°$ *is stressed out.*

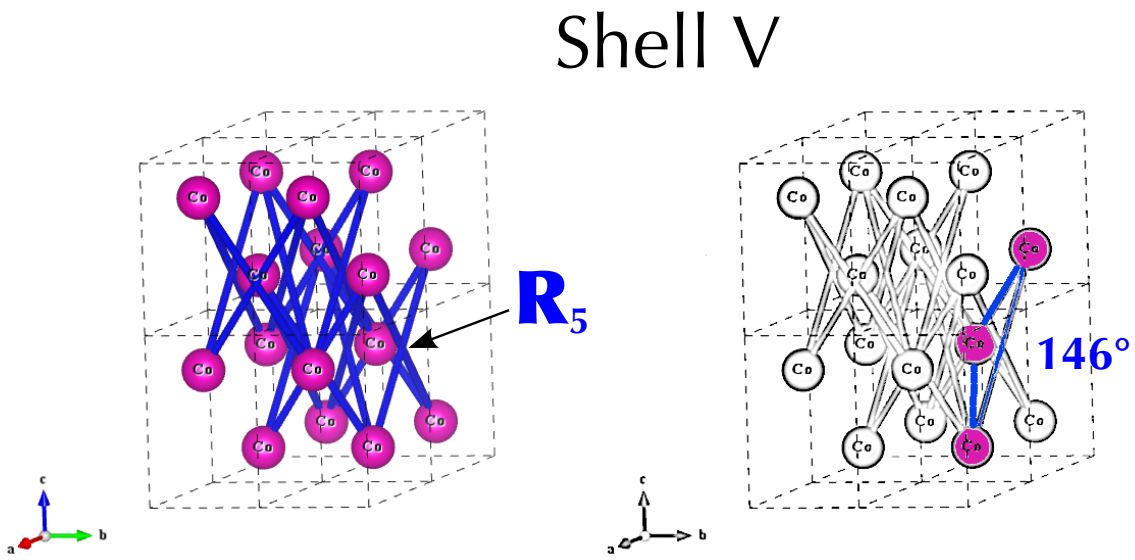

Figure 3.12: *The configuration used for th V shell of the hcp arrangement is sketched. Left panel: the distance is underlined by the arrows. Right panel: The three-body configuration, that involve the* $\theta_3 = 146°$ *is stressed out.*

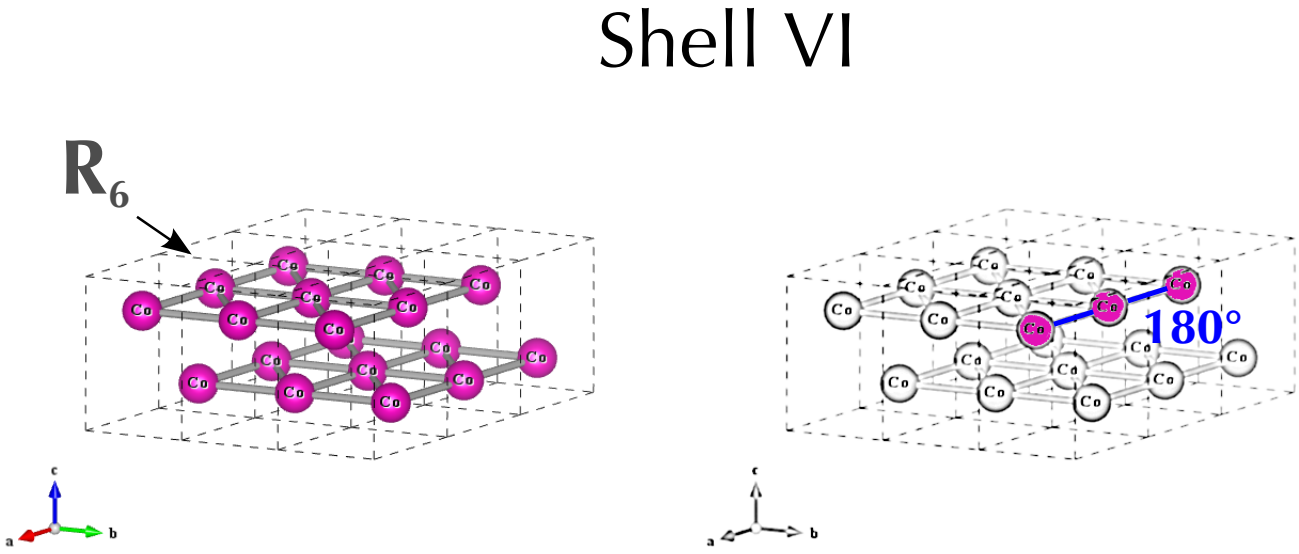

Figure 3.13: *The configuration used for the VI shell of the hcp arrangement are sketched. Left panel: the distance used is underlined by the arrows. Right panel: The three-body configuration, that involve the* $\theta_3 = 180°$ *is stressed out.*

to the shells described from the 3-body term. As a result, the EXAFS analysis of bulk cobalt highlights the importance of the presence of both *hcp* and *fcc* arrangement. To obtain a suitable fit the coexistence of both arrangement is necessary, and subsequently two conditions are tested with respect to the hexagonal arrangement:

- $R_{11} = R_{12}$ that draws an ideal compact packing;
- $R_{11} \neq R_{12}$ that draws a distorted packing that takes into account the possibility of contraction or elongation of the nearest neighbour distance in the c_h direction.

For the analysis of cobalt foil the coordination numbers are fixed at the ideal ones. In the following two sections the results relative to these possibilities are discussed.

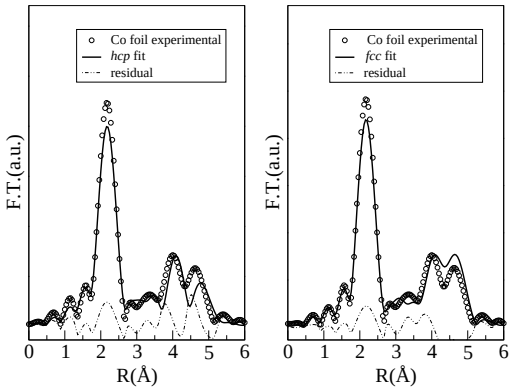

Figure 3.14: *Fourier transform magnitude of the experimental and fitted for two different arrangements. Left panel: Fourier transform magnitude of the experimental and fitted signal obtained using an hcp model. Right panel: Fourier transform magnitude of the experimental and fitted signal obtained using an fcc model. The experimental data and the fitting residual are also shown.*

3.3.4.1 $R_{11} = R_{12}$

When the hexagonal arrangement is built up with $R_{11} = R_{12}$, the obtained fit is shown in fig.3.15. Both the *hcp* and *fcc* component are displayed to stress the different contributions. It is clear that the calculated signal does not suitably fit the positions of the second and third peaks. The single signal components reported in fig.3.16 demonstrate the high importance of the three-body interactions of both phases since some of them are out of phase, for instance the η^{33} *hcp* and the η^{32} *fcc*.

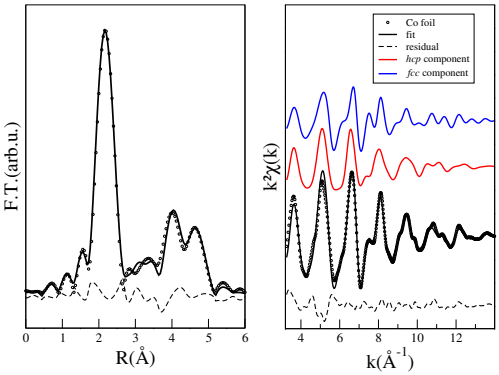

Figure 3.15: *Fit of the EXAFS of bulk cobalt performed in k-space with the $R_{11} = R_{12}$ condition. Left panel: Fourier transform magnitude of the experimental and fitted signals. Right panel: Calculated EXAFS spectrum generated on the basis of the hcp and fcc. The experimental and calculated spectra and the fitting residual are also shown*

.

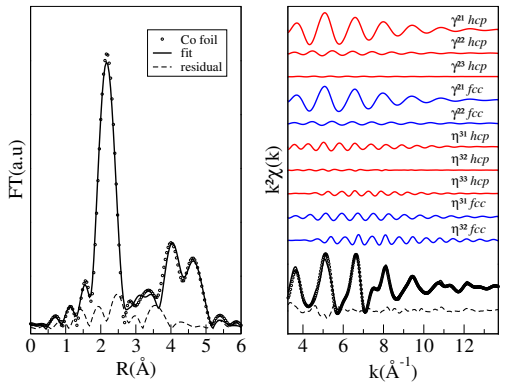

Figure 3.16: *Fit of the EXAFS of bulk cobalt performed in k-space in the $R_{11} = R_{12}$ condition. Left panel: Fourier transform magnitude of the experimental and fitted signal. Right panel: Calculated EXAFS spectrum generated on the basis of the two arrangements. The single signal components of the arrangements, the experimental data and the fitting residual are also shown.*

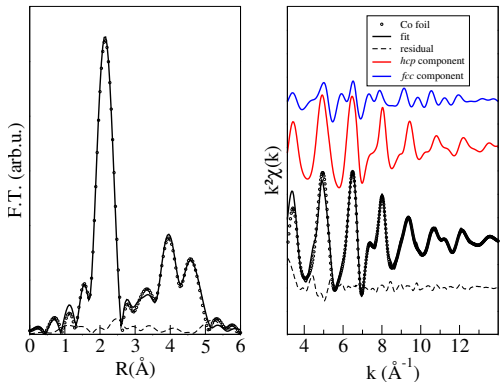

Figure 3.17: *Fit of the EXAFS of bulk cobalt performed in k-space in the $R_{11} \neq R_{12}$ condition. Left panel: Fourier transform magnitude of the experimental and fitted signal. Right panel: Calculated EXAFS spectrum generated on the basis of the two arrangements. The experimental data and the fitting residual are also shown*

3.3.4.2 $R_{11} \neq R_{12}$

The fit obtained with $R_{11} \neq R_{12}$ is shown in fig. 3.17. The R_{12} parameter is calculated with eq.3.6, where *ratio* is a fitting parameter. As it was explained in the 3.3.3 section, the parameter R_{12} is used in the η^3_{11}, η^3_{12} and the η^3_{21} three-body configurations. The fit is improved by allowing the first-neighbour distance splitting, that is a typical feature of the *hcp* bulk metals. When this splitting is included in the model, the positions of the second and the third shells are accurately reproduced. The single signal components are reported in fig.3.18. The condition $R_{11} \neq R_{12}$, allowing to achieve a satisfactory fit of the cobalt foil spectrum, is then applied to the EXAFS analysis of the cobalt nanoparticles.

3.3.5 Cobalt samples analysis

3.3.5.1 Unsupported Co nanoparticles

The nanoparticles data are analyzed and fitted by the approach, shown in section 3.3.4.2, that gave good results for the Co foil data. The refined parameters and the calculated coordination numbers are reported, respectively, in table 3.5 and in table 3.6. The nanoparticles samples could, moreover, show an oxide component. According to this consideration, two oxide shells are taken into account to describe the average local environment of cobalt. Then, in the fitting procedure two γ^2 terms relative to the Co-O and the Co-Co distances in cobalt oxide are allowed. These components are particularly important for the EXAFS analysis of the D3 and D4 samples. The low fitting residual for the D3, D4 and D15 samples (fig. 3.19) proves the suitability of the structural model.

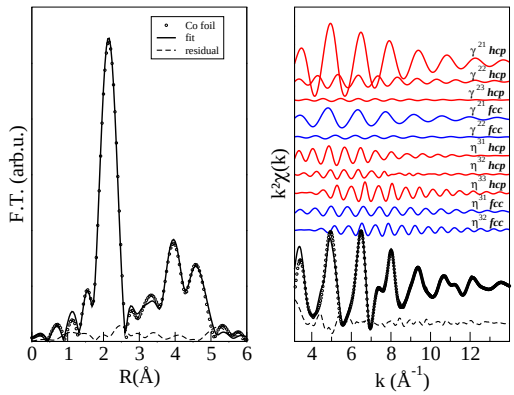

Figure 3.18: *Fit of the EXAFS of bulk cobalt performed in k-space in the $R_{11} \neq R_{12}$ condition. Left panel: Fourier transform magnitude of the experimental and fitted signal. Right panel: Calculated EXAFS spectrum generated on the basis of the two arrangements. The single signal components of the arrangements, the experimental data and the fitting residual are also shown.*

Table 3.4: *Calculated EXAFS parameter for the cobalt foil spectrum in the two tested conditions $R_{11} = R_{12}$ and $R_{11} \neq R_{12}$.*

	$R_{11} = R_{12}$	$R_{11} \neq R_{12}$
$\%_{hcp}$	58	78
$\%_{fcc}$	42	22
a_h (Å)	2.45	2.48
c_h Å)	4.18	4.00
a_c (Å)	3.53	3.57
R_{12} (Å)	-	2.46
$ratio$	1.000	0.993
θ_{1hcp} (°)	138	127
θ_{2hcp} (°)	153	155
θ_{3hcp} (°)	184	183
θ_{1fcc} (°)	121	117
θ_{2fcc} (°)	180	179
$R - factor$	$3.009 * 10^{-5}$	$2.057 * 10^{-5}$

3.3.5.2 Supported Co nanoparticles

The model previously described is also used to simulate EXAFS spectra of supported samples. The refined parameter and the calculated coordination numbers are summarized, respectively in table 3.7 and in table 3.8. For the samples that show an oxide component the γ^2 terms of Co-O and Co-Co distances are allowed.

3.4 Conclusion

The results of the EXAFS analysis demonstrate that both hexagonal and cubic close packing sequences are necessary to obtain a satisfactory fitting to the experimental data. Although the coexistence of typical distances of both *hcp* and *fcc* is witnessed, the EXAFS analysis gives no knowledge on the presence of the layer sequences in two different phases. The results are in agreement with the XRD analysis (chapter 4) as concern the phase amounts. Regard the unsupported samples, the D15, that is prepared with mesytilene as solvent, shows the highest *fcc* component. The D3 and D4 samples, that are prepared with heptane, a solvent with a boiling temperature lower than mesytilene, show a larger amount of hexagonal sequences with respect to D15. Since the hexagonal arrangement is the most stable at room temperature, the amount of cubic arrangement is probably due to the higher syn-

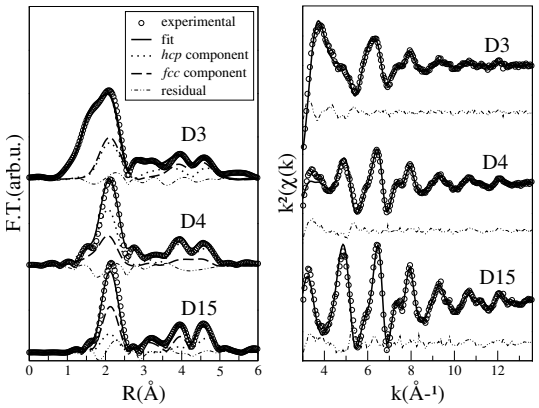

Figure 3.19: *Left panel: Fourier transform magnitude of the experimental and fitted signal for normalized D3, D4 and D15 data. The fitting residual and components of the arrangements are also shown. Right panel: Calculated EXAFS spectrum generated on the basis of the two arrangements. The experimental data and the fitting residual are also shown.*

Table 3.6: *A summary of average coordination numbers of unsupported nanoparticles calculated from Borowski's equation. The ideal coordination numbers are also shown.*

	N_i	D15	D3	D4	Ref
hcp	N_1	10.81	11.22	5.21	12
	N_2	5.99	6.88	3.19	6
	N_3	1.66	1.61	0.74	2
	N_4	14.45	13.16	6.09	18
	N_5	9.39	8.29	3.83	12
	N_6	4.61	4.01	1.86	6
fcc	N_1	7.42	5.66	14.40	12
	N_2	5.99	1.95	5.60	6
	N_3	8.86	5.44	18.00	24
	N_4	4.51	3.29	8.95	18

thesis temperature although for bulk cobalt the phase transition from the *hcp* to the *fcc* arrangement takes place at higher temperature (above 477 K). Regard to supported cobalt nanoparticles, the speculations about solvent effects due to the boiling temperature of the solvent are unconvincing, because supported samples are actually prepared with mesytilene, toluen and heptane at room temperature, that is lower than their boiling points. In the case of the supported cobalt nanoparticles, the relative amounts of the cubic and hexagonal arrangements are independent from the nature of the solvent probably because the solvent and the capping agent are less effective than the interaction between nanoparticles and the surface of silicon wafer. It is worth to notice that for some samples the c_h/a_h axial ratio is not equal to the ideal, that is 1.633. In *hcp* metal is not surprising a changing in the c_h/a_h ratio, as a matter of fact it is well-known a typical contraction of the c_h parameter for most of the *hcp* elements of the transition series and an unusually large c_h/a_h ratio for zinc and cadmium. The analysis of bulk cobalt exhibits a c_h/a_h ratio less lower than the ideal. Most of the samples show a c_h/a_h ratio next to the ideal. Notwithstanding, in the case of D15 the results suggest a reduction of a_h in spite of an elongation of c_h. This phenomenon could be awarded to a close link between the first neighbouring distance along the (a_h, b_h) plane and the cubic lattice parameter, a_c. On the contrary, the c_h/a_h ratio for the Co-mes-ODA suggests a reduction of the c_h parameter. The EXAFS analysis of the nanoparticles samples obtained by thermal decomposition allow us to assert that:

- allowing for both of *hcp* and *fcc* arrangements is essential to fit the EXAFS profile;

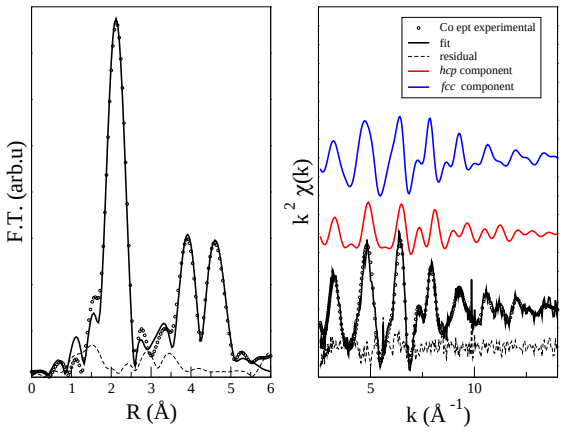

Figure 3.20: *Fit of the EXAFS of Co ept sample performed in k-space. Left panel: Fourier transform magnitude of the experimental and fitted signal. Right panel: Calculated EXAFS spectrum generated on the basis of the two arrangements. The single signal components of the arrangements, the experimental data and the fitting residual are also shown.*

- the reduction of coordination numbers is an evidence of the presence of small particles;
- in the case of unsupported samples the amount of cubic sequences increases when cobalt nanoparticles are prepared using a solvent at higher boiling temperature.

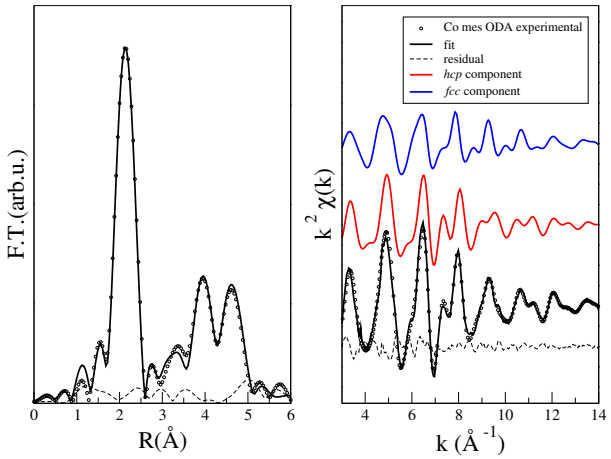

Figure 3.21: *Fit of the EXAFS of Co-mes-ODA sample performed in k-space. Left panel: Fourier transform magnitude of the experimental and fitted signal. Right panel: Calculated EXAFS spectrum generated on the basis of the two arrangements. The single signal components of the arrangements, the experimental data and the fitting residual are also shown.*

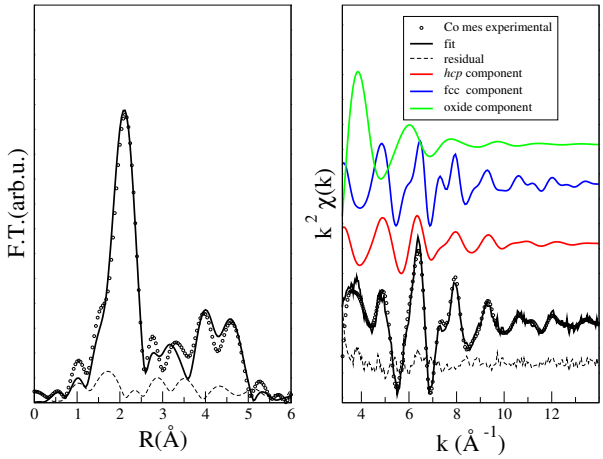

Figure 3.22: *Fit of the EXAFS of Co-mes sample performed in k-space. Left panel: Fourier transform magnitude of the experimental and fitted signal. Right panel: Calculated EXAFS spectrum generated on the basis of the two arrangements. The single signal components of the arrangements, the experimental data and the fitting residual are also shown.*

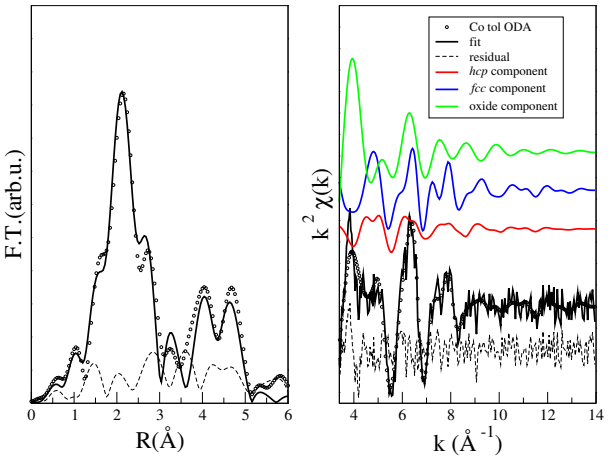

Figure 3.23: *Fit of the EXAFS of Co-tol-ODA sample performed in k-space. Left panel: Fourier transform magnitude of the experimental and fitted signal. Right panel: Calculated EXAFS spectrum generated on the basis of the two arrangements. The single signal components of the arrangements, the experimental data and the fitting residual are also shown.*

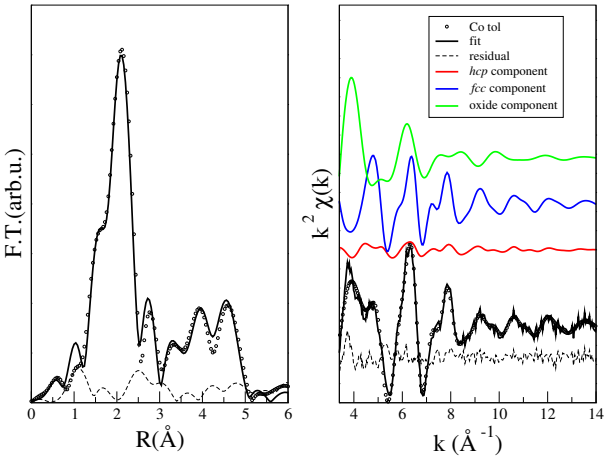

Figure 3.24: *Fit of the EXAFS of Co-tol sample performed in k-space. Left panel: Fourier transform magnitude of the experimental and fitted signal. Right panel: Calculated EXAFS spectrum generated on the basis of the two arrangements. The single signal components of the arrangements, the experimental data and the fitting residual are also shown.*

Table 3.5: *Refined parameter obtained from GnXAS analysis of EXAFS data of unsupported nanoparticles. The lattice parameters, a and c, and the average diameter, $< d >$, are expressed in Å while the angles, θ_1, θ_2 and θ_3 are expressed in degrees (°). The error for lattice parameter is ±0.02, for arrangement percentages is ±20.*

	Co foil	D15	D3	D4
		hcp		
$\%_{hcp}$	78	22	53	35
a (Å)	2.48	2.43	2.47	2.46
σ_{a_h} (Å^2)	0.0019	0.007	0.005	0.004
c (Å)	4.00	4.01	4.02	4.02
σ_{c_h} (Å^2)	0.0019	0.004	0.001	0.002
R_{12} (Å)	2.46	2.45	2.51	2.51
$\sigma_{R_{12}}$ (Å^2)	0.0016	0.001	0.005	0.003
θ_1 (°)	127	123	120	119
θ_2 (°)	155	152	141	152
θ_3 (°)	183	189	171	189
$< d >$ (Å)	-	36	20	20
		fcc		
$\%_{fcc}$	22	78	47	65
a (Å)	3.58	3.53	3.56	3.54
σ_{a_c} (Å^2)	0.001	0.001	0.0011	0.006
R_1 (Å)	2.53	2.50	2.52	2.50
σ_{R_1} (Å^2)	0.0011	0.002	0.002	0.003
θ_1 (°)	117	123	129	124
θ_2 (°)	179	189	186	183
$< d >$ (Å)	-	10	8	10
R-factor	$2.057 * 10^{-5}$	$1.397 * 10^{-5}$	$1.390 * 10^{-6}$	$4.342 * 10^{-6}$

Table 3.7: *Refined parameter obtained from GnXAS analysis of EXAFS data of cobalt supported nanoparticles. The lattice parameters, a and c, and the average diameter, $< d >$, are expressed in Å while the angles, θ_1, θ_2 and θ_3 are expressed in degrees (°). The error for lattice parameter is ±0.02, for arrangement percentages is* ±20.

	Co foil	Co-mes	Co-mes-ODA	Co-tol	Co-tol-ODA	Co-ept
			hcp			
%	78	56	48	11	35	35
a (Å)	2.48	2.48	2.49	2.50	2.51	2.47
c (Å)	4.00	4.13	3.98	4.09	4.10	3.98
R_{12} (Å)	2.46	2.54	2.51	2.39	2.64	2.49
θ_1 (°)	127	121	120	113	123	120
θ_2 (°)	155	151	144	142	146	149
θ_3 (°)	183	188	190	189	189	189
$< d >$ (Å)	-	8	26	30	36	25
			fcc			
%	22	44	52	89	65	65
a (Å)	3.58	3.54	3.55	3.56	3.55	3.54
R_1 (Å)	2.53	2.50	2.51	2.52	2.51	2.50
θ_1 (°)	117	121	128	121	121	125
θ_2 (°)	179	189	190	189	188	188
$< d >$ (Å)	-	18	8	20	40	10

Table 3.8: *A summary of average coordination numbers of supported nanoparticles calculated from Borowski's equation. The ideal coordination numbers are also shown.*

		Co-mes	Co-mes-ODA	Co-tol	Co-tol-ODA	Co-ept	Ref.
hcp	N_1	6.35	10.28	6.35	10.79	10.32	12
	N_2	5.97	6.00	5.97	6.00	6.00	6
	N_3	0.53	1.55	0.53	1.66	1.53	2
	N_4	2.74	13.03	2.74	14.35	13.00	18
	N_5	1.19	8.36	1.19	9.32	8.32	12
	N_6	0.45	4.08	0.45	4.58	4.07	6
fcc	N_1	9.47	6.48	9.47	10.89	7.80	12
	N_2	4.21	2.22	4.21	5.21	3.05	6
	N_3	15.34	6.18	15.34	20.12	9.86	24
	N_4	7.35	3.76	7.35	9.87	4.90	18

Chapter 4

X-Ray Diffraction

4.1 Description of the XRD model

Inspection of representative XRD patterns of nanocrystalline cobalt shows that in most cases the peaks characteristic of the *hcp* and *fcc* cobalt arrangement are simultaneously present. Moreover, it is usually observed a peak broadening depending of the Miller indexes, that addresses to stacking fault disorder.

Therefore, the structure of cobalt nanophases is modelled on the basis of the the following assumptions:

- the *Basic Strucutural Unit* (BSU) is a disk-shaped layer referred to two hexagonal axes $\mathbf{a_h}$ and $\mathbf{b_h}$; Co atoms are placed in the cell origin (fig.4.1);
- the parent stack is built by overlapping the structural units along the $\mathbf{c_h}$ axis ($\mathbf{c_h} \perp \mathbf{a_h}$ and $\mathbf{c_h} \perp \mathbf{b_h}$). Then, the interatomic vectors of the parent stack are given by:

$$\mathbf{t_{klm}} = k\mathbf{a_h} + l\mathbf{b_h} + m\mathbf{c_h} \tag{4.1}$$

  where k, l, m are integers;
- any crystallite of the powder sample is obtained by the translation in the $(\mathbf{a}_h, \mathbf{b}_h)$ plane of the BSU's of the parent stack. Only the smallest shift vectors are allowed;

$$\mathbf{t_A} = -\frac{1}{3}\mathbf{a_h} - \frac{1}{3}\mathbf{b_h}; \tag{4.2}$$

$$\mathbf{t_B} = \frac{1}{3}\mathbf{a_h}; \tag{4.3}$$

$$\mathbf{t_C} = \frac{1}{3}\mathbf{b_h}; \tag{4.4}$$

  Then, a given crystallite is characterized by the sequence of translation vectors of BSU's from the respective starting positions in the parent stack ($\mathbf{t_A}$ $\mathbf{t_B}$ $\mathbf{t_C}$ ... or simply ABC...). To ensure close packing, th sequence of two identical shift vectors(for instance $\mathbf{t_A t_A}$) is not permitted;
- provided that close packing is fulfilled, the relative position of BSU's is rules by a statistical law. It is assumed that each BSU extends its influence as far as the third neighbour, according to the following transition probability matrix 4.1.

Following the formalism of Kakinoki and Komura, the element p_{ij} of the matrix $\mathbf{P}$ give the probability that the triplet of layers heading the i-th row is con-

Table 4.1: *The $\mathbf{P}_{ij}$ matrix elements gives the probability of transition from the i-th to the j-th triplet*

	ABA	ABC	ACA	ACB	BCB	BCA	BAB	BAC	CAC	CAB	CBC	CBA
ABA							$1-\alpha$	α				
ABC					β	$1-\beta$						
ACA									$1-\alpha$	α		
ACB											β	$1-\beta$
BCB											$1-\alpha$	α
BCA									β	$1-\beta$		
BAB	$1-\alpha$	α										
BAC			β	$1-\beta$								
CAC			$1-\alpha$	α								
CAB	β	$1-\beta$										
CBC					$1-\alpha$	α						
CBA							β	$1-\beta$				

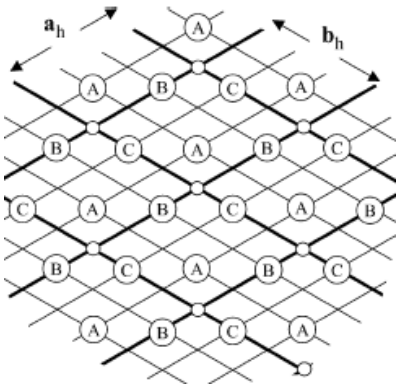

Figure 4.1: *Section along the $(\mathbf{a}_h, \mathbf{b}_h)$ plane of the hexagonal reference stack. The $\mathbf{c}_h$ is perpedicular to the $(\mathbf{a}_h, \mathbf{b}_h)$ plane. The A,B, and C site are the projections of the allowed atomic positions.*

catenated with the triplet heading the j-th column; that is, non-null elements are those for which the last two layers of the row are identical with the first two layers of the column [71][72]. The frequency of occurrence of the j-th triplet is given by

$$f_i = \sum_{j=1}^{12} f_j P_{ij}, \quad {}_{i=1,2,...12} \tag{4.5}$$

Solving the linear homogeneous system 4.5 yields

$$f_i = \frac{\beta}{6(\alpha+\beta)}, \quad {}_{i=1,3,5,7,9,11} \tag{4.6}$$

$$f_i = \frac{\alpha}{6(\alpha+\beta)}, \quad {}_{i=2,4,6,8,10,12} \tag{4.7}$$

The transition probabilities between m-neighbouring BSU are defined by the elements of the $\mathbf{P}^m$ matrix:

$$\mathbf{P}^m = \mathbf{P} * \mathbf{P}^{m-1}, \mathbf{P}^0 = 1 \tag{4.8}$$

and the corresponding relative positions in the $(\mathbf{a}_h, \mathbf{b}_h)$ plane are given by:

$$\mathbf{t}_{ij} = \mathbf{t}_j - \mathbf{t}_i, \quad {}_{i,j=1...12} \tag{4.9}$$

where $\mathbf{t}_j$ and $\mathbf{t}_i$ are the shift vectors (eq.4.4) of the respective BSU triplets. The relative position of two atoms belonging to the m-neighbouring BSU is then:

$$\mathbf{r}_{klm}^{(mn)} = \mathbf{r}_{klm} + \mathbf{t}_{ij} \tag{4.10}$$

where $\mathbf{r}_{klm}$ is given by the eq.4.1 and $\mathbf{t}_{ij}$ by the eq.4.9. The averaged contribution to the overall intensity by this couple of scatterers is:

$$I^{(klm)} = \sum_i j \tag{4.11}$$

The overall intensity is the calculated by summing up all the above terms, for all the interatomic parent stack r_{klm} distances weighted by the respective multiplicity $\mu(r_{klm}$. For the cylindrical parent stack:

$$\mu(r_{klm}) = \frac{1}{a_h b_h c_h(\sqrt{3}/2)} 2r^2 \big[\frac{\pi}{2} - \frac{r_{klm}}{2r} \sqrt{1-(\frac{r_{klm}}{2r})^2} - \arcsin\frac{r_{klm}}{2r}\big][h - c_h m] \tag{4.12}$$

where r is the cylinder radius and h the height. Size distribution is taken into account by averaging over cylindrical particles, all having the sameh/r ratio and weighted by a lognormal function. The possibility that the relative position of two neighbouring scattterers can be distributed around an average value and that this uncertainty propagates to larger distances can also be taken into account. In particular, the function $\exp\left[-2\pi^2 q^2 \sigma^2\right]$, where σ represent the spread of the distribution and increases linearly with the distance between scatterers [26] multiplies each intensity term. Summarizing the XRD patterns have been analysed by a structural model allowing for:

- stacking faults extending their statistical influence as far as the third neighbouring atomic planes;
- microstrains;
- particle size distribution.

The model was fitted to the HrXRD data by a suitable modification of the Debye formula [26].

4.2 Discussion about the model

The probability sequences are independent of the size. This implicit assumption can be a rough approximation, as it is well known that the structure of very small particles can be a function of their size. Of course, the assumption made in this paper is somewhat obliged by the fact that the experimental data do not allow a significant refinement of independent stacking fault probabilities for each size allowed to build a given calculated pattern. On the other hand, it could be acknowledged that on a limited size range this assumption could not dramatically affect the results. Moreover, there is no evidence in the data of a bimodal distribution that could involve different stacking sequences (and eventually support a model allowing for two phases, one predominantly cubic and the other with more frequent hexagonal sequences). The choice of the cylindrical shape is clearly a matter of convenience. In a paper on the structure of gold nanoparticles [26], a noticeable computational effort was made to formulate a model of spherical particles, that is suitable for particles weakly interacting with the environment. On the other hand, an XRD pattern, in the size range of interest, does not allow to discriminate between sphere and isometric cylinder, even for ordered structure. For disordered structures the possibility of shape discrimination is then completely unfeasible. Reference to cylindrical shape has the further advantage of allowing for anisometric shape, such as a flat disk, that could be predominant in the case of, say, a strong interaction with a support.

4.3 Experimental details

High resolution X-ray diffraction (XRD) patterns were recorded at the ID31 diffractometer of the European

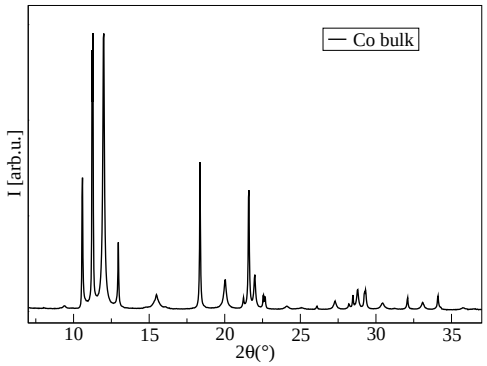

Figure 4.2: *XRD pattern of the bulk cobalt measured at ID31 of ESRF (European Synchrotron Radiation Facilities) at the $\lambda = 0.40000$. The datum proves the coexistence of the hcp and the fcc phases*

.

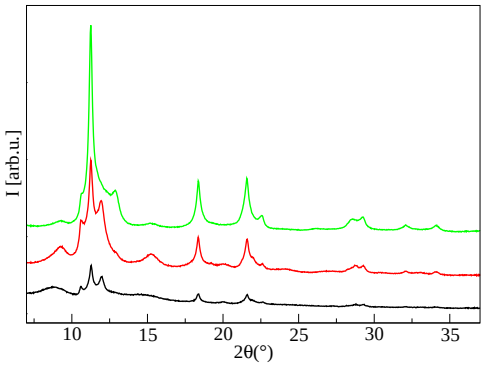

Figure 4.3: *XRD patterns, shifted along the y-axis for sake of clarity, of the nanoparticles of cobalt measured at ID31 of ESRF at the $\lambda = 0.40000$. The datum proves the coexistence of the hcp and the fcc phases and high amounts of stacking faults*

Synchrotron Radiation Facility (ESRF, Grenoble) in trasmission geometry with incident wavelength $\lambda = 0.40000$. The samples were loaded in $0.6mm$ glass capillaries. The diffracted radiation was measured in the $2° - 38°2\theta$ range with a constant scanning speed. A reference Co powder pattern was also collected in the same conditions. The data analysis is carried out with the model previous described in the section 4.1.

4.4 Sample analysis

In fig.4.2 and in fig.4.3 are shown the collected patterns, respectively, of the bulk cobalt and of the cobalt nanoparticles. The profile of the reference metallic cobalt witness the coexistence of both *hcp* and of *fcc* sequences. The XRD patterns of the samples, reported in Figure 4.3, show evidence of cubic and hexagonal sequences and also of an amorphous cobalt oxide phase, which is easily identified by the peak at about 9.4°. According to a qualitative XRD data analysis, the samples prepared with heptane are more oxidized than those prepared with mesytilene. The experimental pattern are analysed with our model, previously described, that allows the quantitative analysis of the crystalline phases present in a powder . The background function is calculated using the Tchebyshev polynomials that allow to reproduce the oxide component. Since the present oxide does not exhibit a crystalline phase we could simulate this contribution to the pattern with polynomials. The best fits are shown in fig.4.4, in fig.4.5 and in fig.4.6.

Due to the fact that the *hcp* and *fcc* cobalt arrangement are simultaneously present in term of probabilistic events, the percentages of the *hcp* and *fcc* arrangement are calculated as a function of α and β. The f_{hcp} and f_{fcc}, reported in eq.4.13-4.14 are the

Table 4.2: *Result form the best fits of the HrXRD patterns. R , the average nanoparticle radius, and the lattice parameters, a and c, are expressed in Å.*

	D15	D3	D4
α	0.337	0.132	0.136
β	0.196	0.229	0.236
h/r	1.1323	1.1036	1.1014
a (Å)	2.5075	2.5075	2.5077
c (Å)	4.0848	4.0720	4.0782
R (Å)	25.5	29.0	31.1

.

Table 4.3: *Percentages of the hcp and fcc arrangement calculated from the frequencies formulas.*

	D15	D3	D4
% *hcp*	37	64	64
% *fcc*	63	36	36

frequencies of the, respectively, the *hcp* sequences and *fcc* sequences of layers.

$$f_{hcp} = \frac{\beta}{6(\alpha+\beta)}) \tag{4.13}$$

$$f_{fcc} = \frac{\alpha}{6(\alpha+\beta)}) \tag{4.14}$$

The calculated percentage are reported in table 4.3. Bearing in mind that plotted size distributions are lognormal functions of the radius of the cylindrical base of the particles, the average radius, R, (table 4.2) is calculated as follow:

- from the size distribution is calculated the volume distribution;
- the average volume is solved with the numerical integral of the volume distribution function;
- the average radius is calculated as the equivalent radius of the sphere with the same average volume.

The so-obtained average radii are in agreement with the TEM measurements, therefore, this result witnesses that the cylindrical model allow to extract the same knowledge about size of nanoparticle than a spherical model spending a lower computing time.

In conclusion, the proposed model fits very well to the experimental patterns of quite different samples showing or a prevalent *fcc* or *hcp habitus*. The structural analysis that can be found in the literature on cobalt makes reference in most cases to two distinct *fcc* or *hcp* phases, simultaneously present in the investigated samples [43][44][45], affected by stacking faults. In the paper by Sort et *al.* the Warren's analysis is carried out only on the *hcp* phase, that is considered largely predominant [43]. In line with this approach, one could also conceive a fitting procedure involving two simulated patterns, both affected by stacking faults according to the Warren's statistical analysis: probably, from a mere numerical point of view, the fitting could be also satisfactory. However, it should also be considered that the cited papers present similar XRD patterns from samples obtained by different synthetic routes ranging from thermal decomposition of precursors to ion implantation [45] etc. Then, the similarity of the synthesis products seems to be ascribed to some inherent property of the cobalt metal structure rather than to a lack of control on synthesis products, giving rise to two distinct allotropic phases. The problem of the most suitable structural model for cobalt has evident important consequences on the correlation between structure and magnetic properties, as recognized in particular by Sort [43].

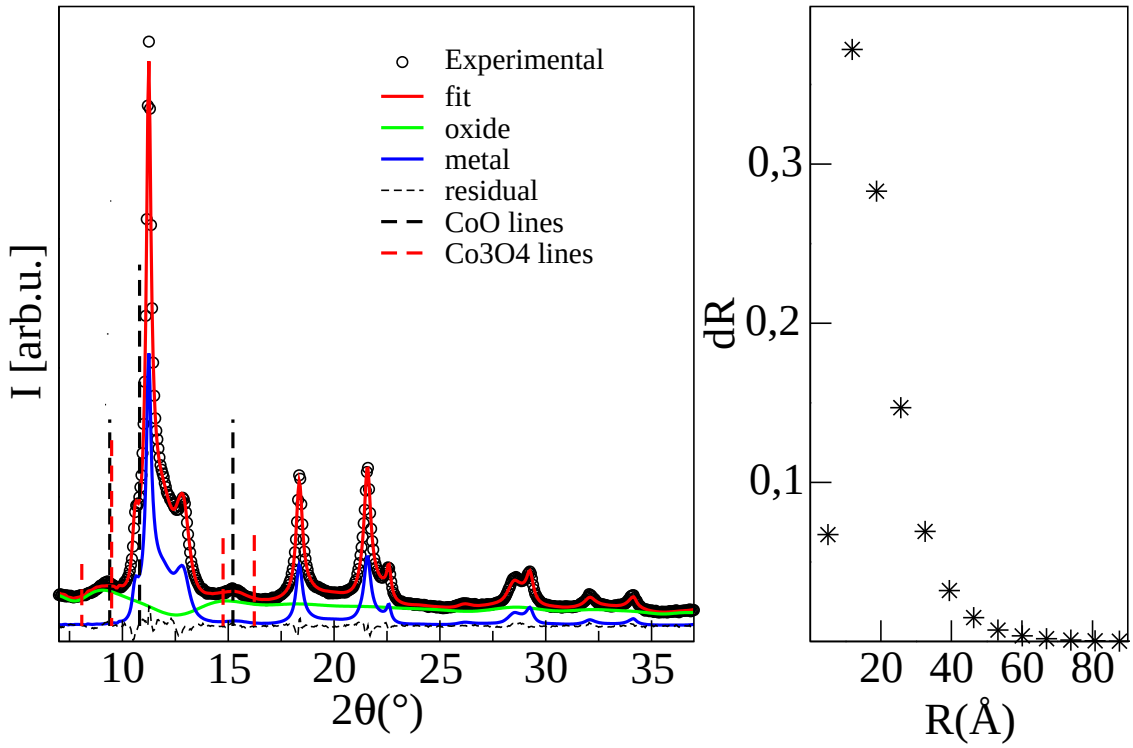

Figure 4.4: *Left panel: XRD fit of the D15 sample obtained using the model described in the section 4.1. Right panel: The size distribution function of the nanoparticles of the D15 sample*

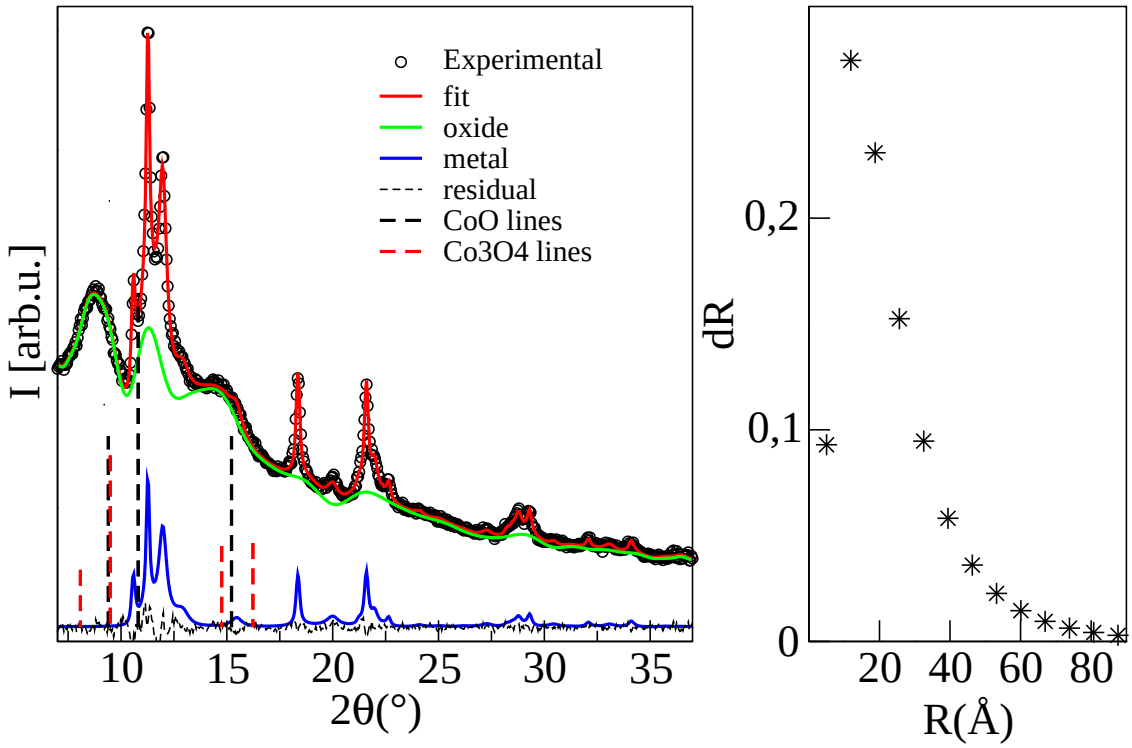

Figure 4.5: *Left panel: XRD fit of the D3 sample obtained using the model described in the section 4.1. Right panel: The size distribution function of the nanoparticles of the D3 sample*

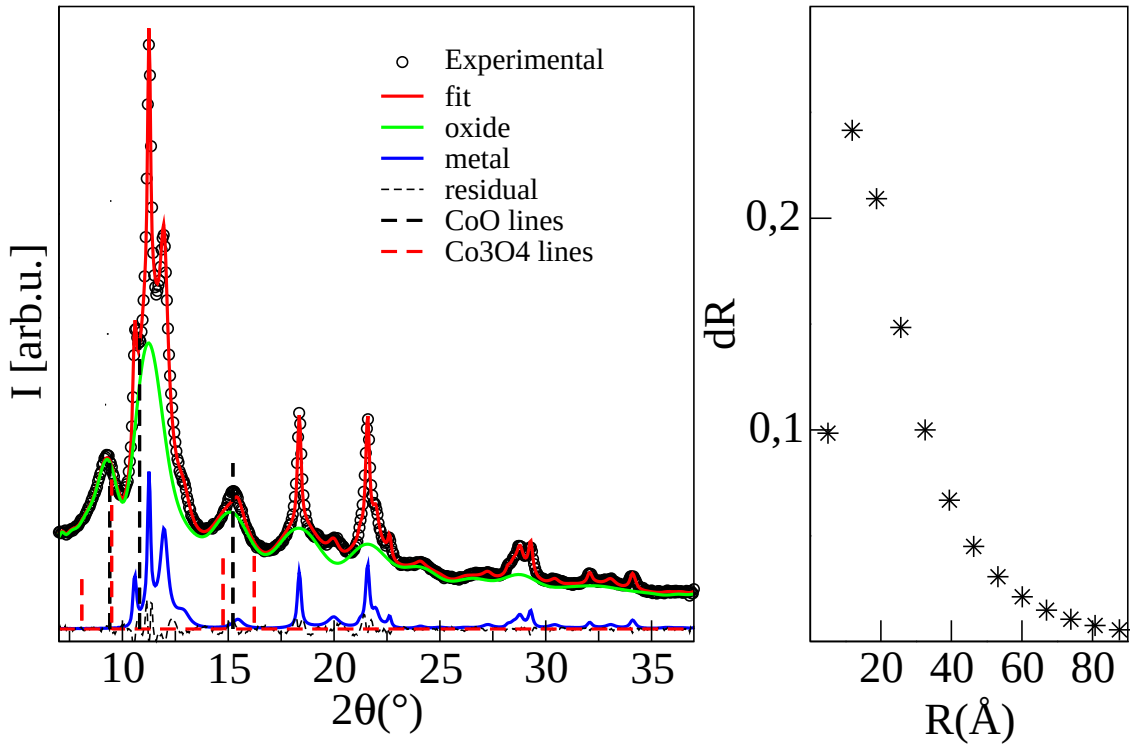

Figure 4.6: *Left panel: XRD fit of the D4 sample obtained using the model described in the section 4.1. Right panel: The size distribution function of the nanoparticles of the D4 sample*

Chapter 5

Atomic Force Microscopy

5.1 A brief history of scanning microscopies

The first scanning microscopy technique that reached technological maturity is the Scanning Electron Microscopy (SEM) whose earliest commercial instrument was delivered in 1965 by Cambridge Instruments. The technique exploits a nanometer sized electron beam to scan the sample surface; the image of the surface is obtained by measuring the distribution map of the intensity of the signal emitted from the specimen scanned area, as a result of the interaction with the electron beam. SEM reaches a magnification of about six orders of magnitude and, like all techniques involving an electron probe, requires ultra high vacuum environment. Moreover, to avoid accumulation of electrostatic charge, the specimen surface must be conductive.

The Scanning Tunneling Microscopy (STM) was invented in 1982 by Binnig and Rohrer at IBM Zurich [73]. A tiny metal tip connected to a cantilever scans the sample surface and exploits the electron tunnel effect to reconstruct, by cantilever deflection, the image of the specimen surface. For materials unable to conduct a tunneling current, in 1986 Gerd Binnig invented the atomic force microscope (AFM) [74] [75]. In AFM microscopy the scanning tip is sensitive to the van der Waals interactions with the sample surface. Due to the fact that AFM could be applied to a large variety of materials (biological, diluted, perishable...), this technique received great attention from the scientific community. Samples can be analysed in different environments such as air, liquids or vacuum. The only mode available for imaging was initially the contact mode, using the scanning tip in close contact with the sample surface: even if it is the simplest mode and still an extremely powerful and useful technique [76], this mode limited the type of samples that could be examined. Nowadays, other modes of AFM operation are available.

Non-contact mode was first introduced in 1987 by Martin *et al.* [77]. In non-contact mode the cantilever oscillates at a small distance (1-10 nm) above the surface. Because the forces on the sample are much lower than in contact mode, even the softest samples can be imaged without damage. This is the case of the biological samples that in contact mode, due to specimen softness, can be easily damaged .

In 1987 the magnetic force microscopy (MFM) was also demonstrated by Martin and Wickramasinghe [78]. The technique is based on a force microscope to measure the magnetic force between a magnetized tip and the scanned surface. The tip scans the sample surface to detect the magnetic domain structure of the sample achieving to a resolution of about 30 nm. Both AFM and MFM are used in this thesis.

5.2 Apparatus and experimental details

The wide variety of experiments that can be performed with an AFM apparatus make it a powerful tool to analyse and characterize samples at microscopic level. In principle, an Atomic Force Microscopy (AFM) apparatus is a relatively simple instrument. Its main components are the microscope stage and the control electronics. As usual in today's technology, input/output and instrument control are managed by an interfaced computer. The microscope stage contains the scanner, that is the mechanism for moving the AFM tip, a sample holder and a force sensor, to hold and monitor the AFM tip. The details of a surface can be investigated with very accurate resolution ranging from $100\mu m$ to less than $1\mu m$. The tip, of nanometric diameter and $2 - 15\mu m$ length, is located at the end of a $200\mu m$ to $400\mu m$ long cantilever. In order to maintain the tip at a constant height above the sample a feedback mechanism is used. During the scan of the sample different forces attract or repel the tip; the cantilever deflections are collected using a laser diode, and then suitably processed to map the surface image. In an AFM apparatus the attractive force between the tip and the sample is due to Van der Waals interaction while the repulsive force is due to the Pauli force. The tip-surface distance dependence is reported in fig.5.2. Initially, the distance between

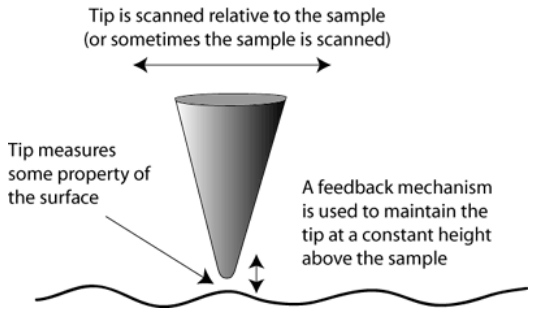

Figure 5.1: *Tip scan the surface measuring properties of the surface while a feedback mechanism is applied.*

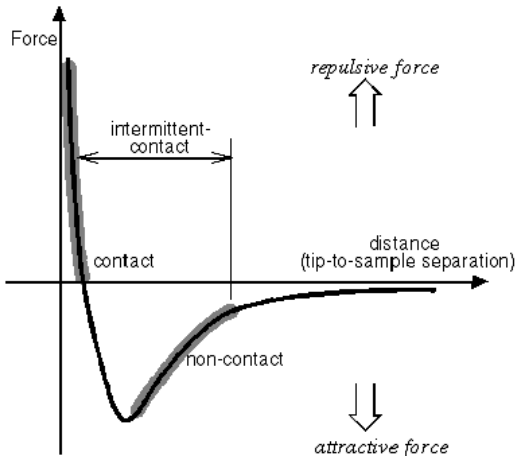

Figure 5.2: *The forces between tip and surface of the sample vs distance contact and non-contact regions are evidenced.*

the tip and the sample surface is set to a large value, so that the force is zero; then, decreasing the distance to tens to hundreds of ångstroms, the cantilever gets the non-contact region where the tip-surface interaction is attractive. In the contact region the force is repulsive and the tip-to-sample distance is less than a

few ångstroms. The design for an optical lever AFM sensor is illustrated in fig.5.3. A laser beam is reflected

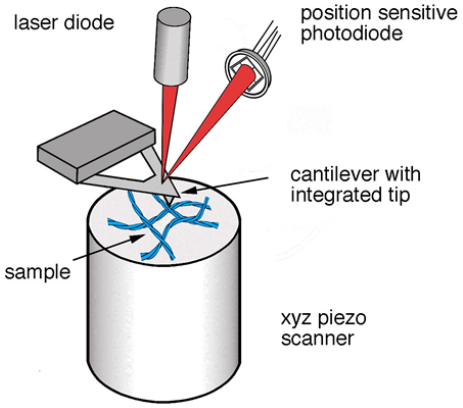

Figure 5.3: *Design of an optical AFM sensor based on the reflection of a laser light.*

by the back side of a reflective cantilever onto a four-segment photodetector. If the tip interacts with the surface, the cantilever is deflected and the light path changes. The force is then measured by monitoring the movement of the reflected light detected by the four quadrants of the photodetector. The resulting image is a topographical representation of the scanned sample surface that has been imaged.

In this work all the images are recorded at the ISMN (Istituto dei Materiali Nanostrutturati) of of the CNR of Bologna in collaboration with Dr. Cristiano Albonetti. The AFM scans, that are constituted of 512x512 points, are collected in ambient air at room temperature with an atomic force microscopy with a scan rate of $0.6Hz$ using silicon cantilevers with a typical curvature radius of the tip of $10nm$, a resonance frequency of approximately $180kHz$, and an elastic constant of $5.6Nm^{-1}$. Sample preparation for AFM is very simple and in general (and also for my sample) there is no need for sample coating, electrical grounding, or sample transparency. The MFM images are collected in the same experimental conditions as the AFM scans with a scan rate of $0.8Hz$ using a silicon cantilever covered of metallic cobalt with a typical curvature radius of the tip of $10nm$, a resonance frequency of approximately $150kHz$, and an elastic constant of $5Nm^{-1}$. The Magnetic force microscopy scans are constituted of two images, one containing the topography of the surface and the other the surface magnetic map. The experimental technique used is called *Two Pass technique*, widely used for magnetic characterization. The sample is scanned twice, in the first scan the topography of the surface is obtained. In the second scan the tip to surface distance is set according to the topography line extracted from the first scan, in order to keep constant van der Waals forces [76]. As a result, the MFM image is not biased by the topography signal.

The data analysis is carried out using the Gwyddion software [79]. The processing steps include the levelling and the subtraction of the background. Actually, the silicon wafer could be tilted and this effect could mask the change in height of the nanoparticles; therefore, a polynomial equation is used to suitably reproduce the inclination of the substrate. The fundamental physical quantities that have been analysed are the average height and the roughness, that is strictly correlated to the height irregularities. Regarding the roughness, two different parameters are taken into account, that is the *roughness average*, R_a, and the *root mean square roughness*, R_q. The latter parameter is defined as the average of the measured height deviations. The R_a and R_q parameters are mathematically expressed by the eqs.5.1-5.2, respectively:

$$R_a = \frac{1}{N}\sum_{j=1}^{N}|r_j| \tag{5.1}$$

$$R_q = \sqrt{\frac{1}{N}\sum_{j=1}^{N} r_j^2} \tag{5.2}$$

Also a grain analysis is carried out in order to obtain the size of the aggregates. To mark the particles the watershed algorithm is employed in order to determine local minima and image segmentation in image processing. The algorithm is briefly described: a virtual water drop is placed, if the the drop is not in a local minimum it follows the steepest descent path to minimize its potential energy. This process is repeated several times. The results is a set of lakes, then the area of each of the lakes is evaluated and the smallest lakes are removed assuming that they originated by noise. The grain so found are marked and the position, the occupied area, and volume of each grain can be determined.

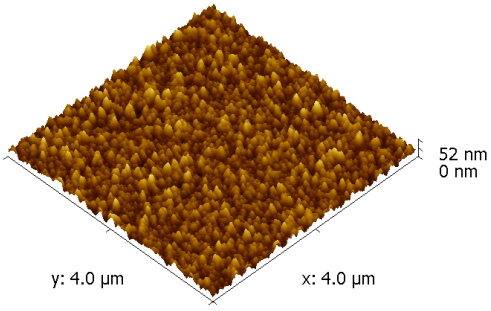

Figure 5.4: *AFM 4µmx4µm of the Au1 sample.*

5.3 Imaging analysis

5.3.1 Morphology of gold film

The AFM images of the gold samples are shown in the appendix B from fig.B.16 to fig.B.19. To analyse the scanned samples the data need a pretreatment consisting in the removal of a polynomial background. Thereafter, the lines of the images are corrected by matching the height median and finally the height zero is fixed. As an example, the 3D image of the Au1 sample is reported in fig.5.4. The average height of supported gold samples is reported in table 5.1. By inspection of table 5.1, it is possible to notice that the mean dimension of the gold nanoparticles deposited on the thermally treated substrate (sample Au4) is smaller than the size of the Au particles deposited on silicon substrates covered by the layer of native-SiO_2. Taking into account the three samples having a different Si dopant concentration, a decrease of the mean nanoparticle size with increasing dopant level can be evidenced. Raffa and coworkers [58] showed that the properties of an Au thin film, specifically the sensing behaviour, strongly depends on the deposition substrate. Furthermore, Hatanaka and coworkers [80], showed that the oxide thickness increased linearly with the dopant concentration, and that this phenomenon has a deep influence on the morphology of the surface. Similar observations were made by Wolkenberg [81], that proposed a relation between the native oxide layer thickness and the concentration of defects of the silicon substrate. The substrate condition plays an important role in the growth of native oxide on silicon. The growth rate of native oxide films is similar for lowly and moderately doped silicon substrates [82]. Among the different defects on the native silica, the most studied are silicon dangling bonds, nonbridging oxygen centers, and silanolate groups that, as it has been recently demonstrated, act as adsorption sites for gold particles [83]. Several theoretical calculations demonstrated that Au particles bind more strongly to a defect-rich surface compared to a defect-free surface,

Table 5.1: *Height function distribution analysis of the gold samples. The average height, $< h >$, and the Full Width at Half Maximum, FWMH of the fitted function distribution, are reported.*

Sample name	$< h >$ (nm)	FWHM (nm)	Grains size (nm)	Doping (cm^3)
Au1	31.5	3.2	22	1.62
Au2	15	7	20	2.35
Au3	16	5.5	20	7.14
Au4	9	6.5	13	0

and that significant charge transfer occurs from the support to the Au particles [84][85][83].

The roughness analysis is carried out on sample areas of $5\mu m$x$5\mu m$ -$3\mu m$x$3\mu m$. In fig.5.5 the roughness, R_q, is plotted as a function of dopant level concentration. A low value of roughness (table 5.2) gives evidence of a homogeneous deposition. Considering

Table 5.2: *Calculated root mean square roughness for the gold supported samples.*

Sample name	scan size (μmxμm)	R_q (nm)
Au1	5x5	5.5
Au1	3x3	7.0
Au2	5x5	4.8
Au2	3x3	6.15
Au3	5x5	5.1
Au3	3x3	6.35
Au4	5x5	3.15
Au4	3x3	4.05

that the roughness and the amount of gold nanoparticles are similar in all the gold samples and that, on

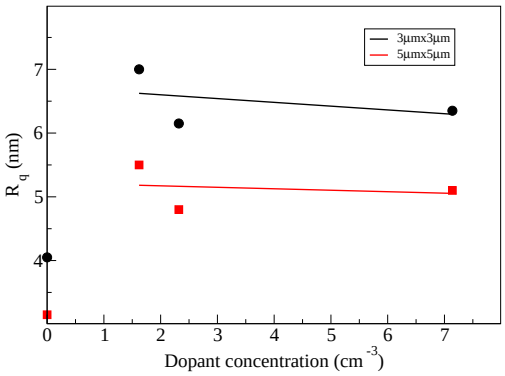

Figure 5.5: *Calculated R_q vs the dopant level of concentration for gold supported samples for $5\mu m$x$5\mu m$ and $3\mu m$x$3\mu m$ images.*

the contrary, the average height is different, it seems appropriate to suppose that the amount of superficial defects and the consequent metal-nanoparticle interaction could play a key role in the aggregation step. Increasing the dopant concentration, the amount of trapping centers increases, and consequently the aggregation of the metal gold subunits, mostly interacting with the superficial defects, is limited.

5.3.2 Morphology of cobalt films

The collected AFM data are shown from fig.B.1 to fig.B.15. The images are pretreated with the procedure described in the previous section (5.3.1). In fig.5.6 the 2D and the 3D images of the Co-mes-ODA sample are reported. In fig.5.7 the height distribu-

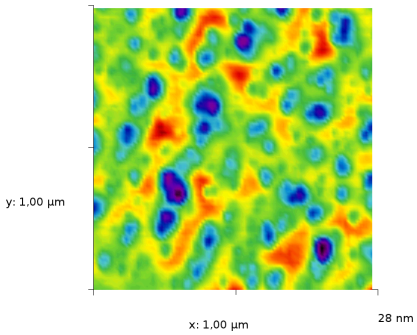

(a)

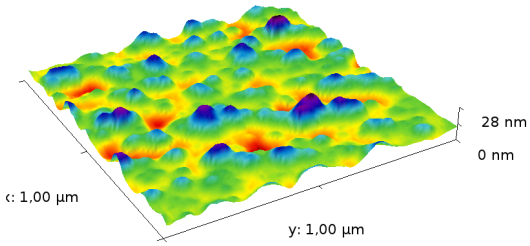

(b)

Figure 5.6: *AFM 3μmx3μm of the Co-mes-ODA sample. (a) 2D image (b) 3D image.*

tion functions calculated from the 3μmx3μm images are drawn. All samples are characterized by a z-distribution in the nanometer range. To extract the average height, a lorentzian fit is performed (fig.5.7)

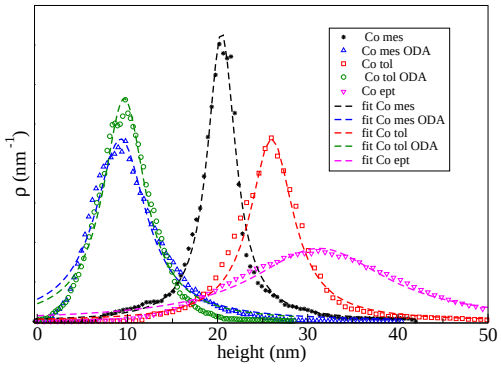

Figure 5.7: *Height distribution functions calculated from the 3μmx3μm images of cobalt supported samples. The height distribution functions of the different Co samples are plotted with symbols and the respective Lorentzian fits with dashed lines, according to the legend.*

and the parameters are reported in table 5.3). An important effect on the distribution function is produced by the capping agent; in fact, both samples prepared with the octadecylamine show a distribution function with similar shape and a close maximum position. With respect to samples synthesized without capping, Co-mes-ODA and Co-tol-ODA are characterized by a smaller average height (table 5.3).

The roughness analysis for the cobalt samples is carried out on 5μmx5μm -3μmx3μm -1μmx1μm images and it is summarized in table 5.4. The cobalt deposition on silicon wafer is homogeneous, as the low values of the calculated R_q demonstrate, in agreement with roughness values of thin films of cobalt on silicon, prepared by electrodeposition [86]. In figure 5.8 the values of R_q vs scan size are plotted. We must bear in mind that each image is constituted of a constant num-

Table 5.3: *Height function distribution analysis of the cobalt supported samples. The average height, h, and the FWMH of the fitted function distribution are reported.*

Sample name	$< h >$ (nm)	FWHM (nm)	Grain size (nm)
Co-mes-ODA	9.3	11.8	19
Co-mes	20.5	3.5	34
Co-tol-ODA	9.6	8.0	19
Co-tol	26	8.3	23
Co-ept	31	82	27

Table 5.4: *Calculated roughness average and root mean square roughness for the cobalt supported samples.*

Sample name	scan size ($\mu mx\mu m$)	R_a (nm)	R_q (nm)
Co-mes	5x5	1.5±0.3	1.9±0.3
Co-mes	3x3	2.0±0.3	2.6±0.4
Co-mes	1x1	3.4±0.7	4.4±1.0
Co-mes-ODA	5x5	2.7±0.6	3.7±1.1
Co-mes-ODA	3x3	3.3±0.4	4.3±0.6
Co-mes-ODA	1x1	3.0±0.5	3.8±0.7
Co-tol	5x5	9 ± 3	12±5.
Co-tol	3x3	3.6±1.3	4.8±1.9
Co-tol	1x1	1.5±0.3	1.9±0.4
Co-tol ODA	5x5	2.9±0.4	3.7±0.6
Co-tol ODA	3x3	2.6±0.4	3.3±0.7
Co-tol ODA	1x1	1.6±0.3	1.9±0.4
Co-ept	5x5	7.5±0.6	9.5±0.7
Co-ept	3x3	7.5±0.7	9.4±0.9
Co-ept	1x1	6.9±0.9	8.5±1.0

ber of pixels, therefore decreasing the scan size, the resolution of the measurement increases. Changing the scan from $5\mu m$x$5\mu m$ to $1\mu m$x$1\mu m$ the roughness of Co-ept, of Co-mes-ODA, and of Co-tol-ODA are constant within the experimental errors. Increasing the resolution of the measure, the R_q of the Co-mes sample slowly raises, whereas the roughness of the Co-tol sample quickly decreases.

The Co-ept and Co-mes-ODA samples have been investigated with MFM using the *Two pass technique* previously described. In fig. 5.10- 5.11 and in fig.5.12-5.13 the topography and MFM images of the same investigated area are shown, respectively, for Co-ept and for Co-mes-ODA in order to measure the magnetostatic force between a magnetic and sample. The component of magnetization in the xy plane is not taken into account in this discussion, as the MFM measurements are sensitive to the component along the z-axis as it is possible to see in fig.5.9. Then, MFM allows to map, in constant height mode, the gradient of the sample field z-component. All reported MFM scans are collected with a tip to surface distance of 50 nm. To exclude that attractive forces, responsible of the topographic map, could affect the magnetic signal, the MFM measurement are carried out with a tip to surface distance higher than the distance at which the attractive force are crucial (below 30nm). Therefore, the obtained images (fig.5.12-5.13) are ascribed to the magnetic behaviour. Due to the same experimental tip to surface distance (50 nm) during Co-ept and Co-mes-ODA scans, the detected magnetic domain structure is comparable. By inspection of MFM scans, a magnetic contrast is clearly individuated in these two samples, that show a predominant amount of metallic component in the XAFS spectra . The Co-mes sample, that show a lower average height $< h >$ (5.3), exhibits a higher perpendicular magnetic contrast, while in the case of Co-ept, although present,

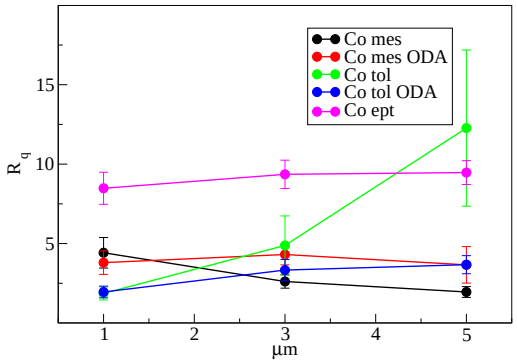

Figure 5.8: *Calculated R_q vs scan size.The errors bars are shown.*

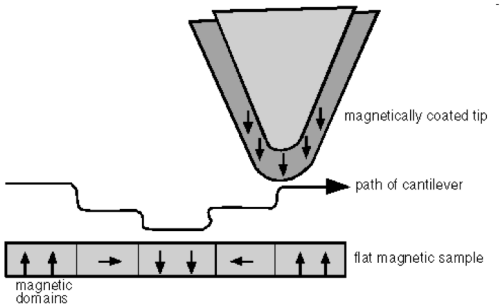

Figure 5.9: *Sketch of the interaction between a flat sample and a magnetic tip.*

the magnetic contrast is lower. Remembering that the magnetic domains of low coercivity samples are mostly wiped out by hard magnetically coated tips, as in our case, the different response to magnetic investigation can be attributed to the different coercivity of the two samples.

h

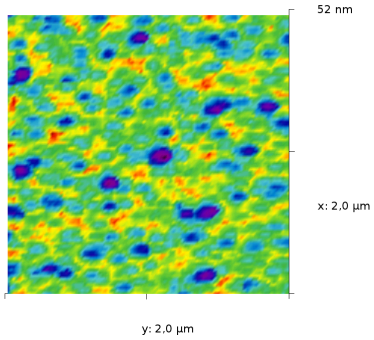

(a)

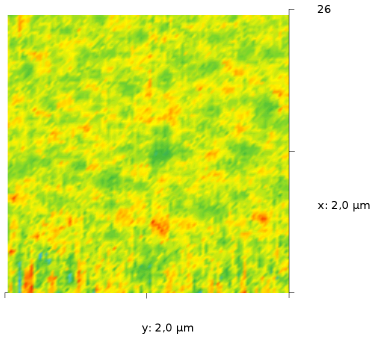

(b)

Figure 5.10: *AFM and MFM $2\mu m x 2\mu m$ of the Co-ept sample. (a) 2D topography. (b) 2D MFM.*

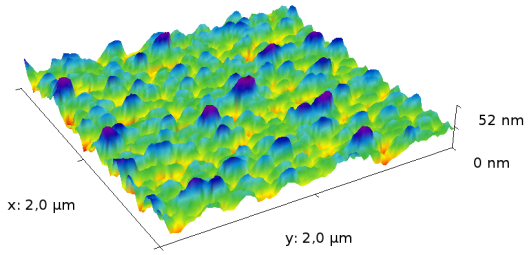

(a)

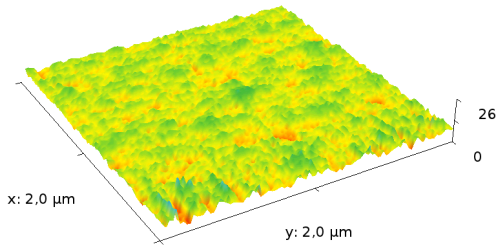

(b)

Figure 5.11: *AFM and MFM 2µmx2µm of the Cocept sample.(a) 3D topography. (b) 3D MFM*

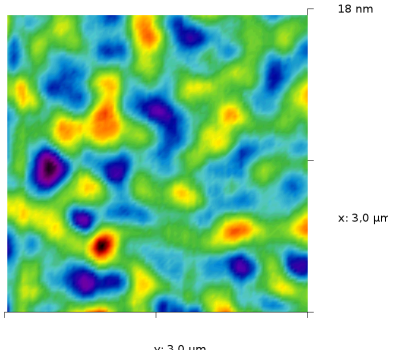

(a)

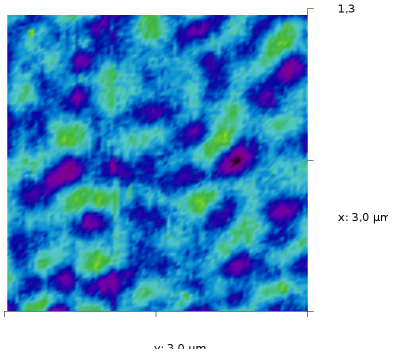

(b)

Figure 5.12: *AFM and MFM 3µmx3µm of the Comes-ODA sample. (a) 2D AFM. (b) 2D MFM.*

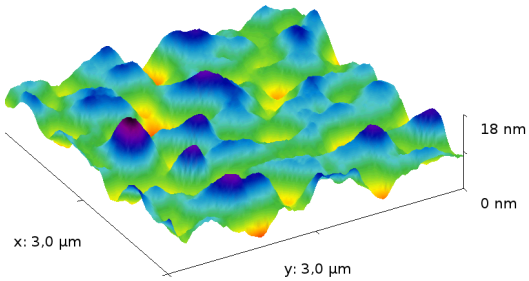

(a)

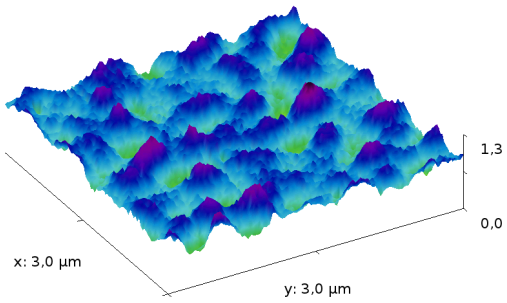

(b)

Figure 5.13: *AFM and MFM 3µmx3µm of the Comes-ODA sample.(a) 3D AFM. (b) 3D MFM*

Chapter 6

GISAXS

The structural studies of surfaces suffered from the lack of surface sensitivity in transmission geometry for long time, because the signal is proportional to the scattering volume. Furthermore, the surface signal is affected by (i) the small cross section for surface scattering, (ii) the photoelectric absorption, and (iii) bulk scattering of the defects. By the use of grazing incidence geometry and by the advantage of synchrotron radiation (high coherence and brilliance) these problems have been overcome. If an x-ray beam hits a surface with an incidence angle below the angle of total external reflection, the wavefield penetration depth is considerably decreased down to a few nanometers, and, as a consequence, the surface or subsurface signal is increased with respect to the volume one. Any discontinuity (surface roughness, islands, inclusions, particles, clusters) scatters either the transmitted or the reflected beam. In addition, for incidence below the angle of total external reflection, the evanescent refracted wave is confined to the top layer and provides a considerable enhancement of surface sensitivity [87]. The use of wavelength between 1 Å and 8 Å enables to study microscopic details of the roughness on comparable length scale [88]. GISAXS (Grazing Incidence Small Angle X-ray Scattering) offers several advantages in spite of microscopies:

- non-invasive technique;
- depth sensitivity by selecting the angle of incidence;
- statistical average that is typical of x-ray measurements;
- measurements that can be performed in several environments (specific gas atmosphere o vacuum).

Nevertheless, the flatness and low roughness are fundamental requisites to carry out a GISAXS experiment and it must be borne in mind that the full potential of GISAXS is realized by using a synchrotron radiation source in combination with two-dimensional detectors. GISAXS theoretical treatment benefited from the development of the Distorted Wave Born Approximation (DWBA). The treatment of x-ray scattering from rough surfaces was introduced by Sinha [88] and Vineyard [89].

6.1 Theory

For a given incoming x-ray beam, the angle of incidence, α_i, the exit angle, α_r, and the transmission angle, α_t, are measured with respect to the sample surface, as reported in the scheme of fig.6.1). To de-

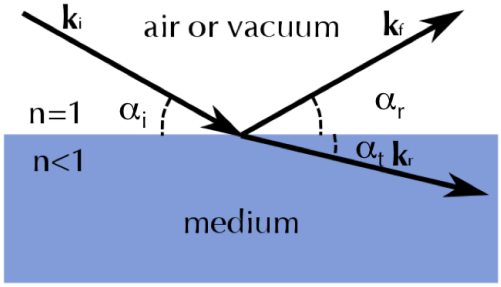

Figure 6.1: *Wave propagation and reflection and refraction of x-ray.*

termine of the reflectivity of a plane x-ray wave at an ideal smooth surface, the Fresnel equations can be used and can be expressed as a function of the grazing incidence angle, α_i, and of the complex refractive index of a medium, n:

$$r(\alpha_i) = \frac{E_r}{E_i} = \frac{\sin\alpha_i - \sqrt{n^2 - \cos^2\alpha_i}}{\sin\alpha_i + \sqrt{n^2 - \cos^2\alpha_i}} \tag{6.1}$$

$$t(\alpha_i) = \frac{E_t}{E_i} = \frac{2\sin\alpha_i}{\sin\alpha_i + \sqrt{n^2 - \cos^2\alpha_i}} \tag{6.2}$$

For small angles the Fresnel reflection and transmission coefficient are approximated [87]:

$$r(\alpha_i) = \frac{E_r}{E_i} = \frac{\alpha_i - \alpha_t}{\alpha_i + \alpha_t} \tag{6.3}$$

$$t(\alpha_i) = \frac{E_t}{E_i} = \frac{2\alpha_i}{\alpha_i + \alpha_t} \tag{6.4}$$

Plainly, the eq.6.1 and eq.6.2 refer to the amplitude of the electric field. The coefficient R and T for the reflected and transmitted intensity are respectively:

$$R(\alpha_i) = \frac{I_r}{I_i} = |r|^2 \tag{6.5}$$

$$T(\alpha_i) = \frac{I_t}{I_i} = |t|^2 \tag{6.6}$$

The interaction of x-rays with matter can be described in a classical way by the index of refraction n. The ratio of the refractive indices of two different media determines the angle of refraction, α_t by Snell's law:

$$n_i \cos\alpha_i = n_t \cos\alpha_t \tag{6.7}$$

where n_i and n_t are the index of refraction of the vacuum and of the medium, respectively. The index of refraction $n = \frac{n_t}{n_i}$ is written in terms of the complex atomic scattering factor $f = f_1 - if_2$

$$n = 1 - \delta + i\beta = 1 - \frac{(\rho_a r_0 \lambda^2)}{2\pi}(f_1 - if_2) \tag{6.8}$$

where λ is the wavelength, ρ_a is the number density of atoms and r_0 is the classical electron radius. For incident-angles below the critical angle, α_c, it comes to total external reflection, or rather, when the refraction angle is zero, a critical angle, α_c, is defined.

$$\alpha_c \approx \sqrt{2\delta} \tag{6.9}$$

In the energy region away from the absorption edges, δ is a positive quantity for all elements, so the real part of the refractive index is smaller than unity, and therefore the total reflection of x-rays can be observed in the region of incident angles below the critical angle [90]. In the eq.6.8 δ, related to the dispersion, is the real part of the refractive index and is written as

$$\delta = \frac{(\rho_a r_0 \lambda^2)}{2\pi} f_1 \tag{6.10}$$

β is the imaginary part and represent the absorption component:

$$\beta = \frac{(\rho_a r_0 \lambda^2)}{2\pi} i f_2 \tag{6.11}$$

For small angles the Taylor expansion of $\cos\alpha_i$ in eq.6.7 leads to

$$\alpha_i^2 = \alpha_t^2 + 2\delta - 2i\beta = \tag{6.12}$$

$$= \alpha_t^2 + \alpha_c^2 - 2i\beta \tag{6.13}$$

Therefore the eq.6.5 is rewritten as:

$$R = \left| \frac{\alpha_i - \sqrt{\alpha_i^2 - \alpha_c^2 + 2i\beta}}{\alpha_i + \sqrt{\alpha_i^2 - \alpha_c^2 + 2i\beta}} \right|^2 \quad (6.14)$$

The amplitude of the scattered wave in the DWBA can be written as:

$$A(\mathbf{q}) = \frac{k^2}{4\pi} \int \mathbf{E}^{out}(\mathbf{r}) \chi_0(\mathbf{r}) \mathbf{E}^{in} dV \quad (6.15)$$

$\mathbf{E}^{in}$ and $\mathbf{E}^{out}$ are the wave field in the scattering object produced by x-ray plane waves incoming and outgoing, respectively and $\chi_0(\mathbf{r})$ is the disturbance of the dielectric polarizability, and k is the modulus of the wave vector in vacuum. In case of GISAXS the wave field $\mathbf{E}^{in}$ and $\mathbf{E}^{out}$ can be calculated by the Fresnel equation (eq.6.1-6.2). In addition to a normal scattering event, four additional events must be taken into account with the Distorted Wave Born Approximation (DWBA).

(*1*) direct diffuse scattering from the nanoparticles;

(*2*) diffuse scattering from the nanoparticles followed by specular reflection from the surface;

(*3*) specular reflection from the surface followed by the diffuse scattering from the nanoparticles;

(*4*) specular reflection from the surface followed by diffuse scattering from the nanoparticles followed by specular reflection from the surface.

The diffuse scattering cross section can be written:

$$\frac{d\sigma}{d\Omega}(\mathbf{q}_{||}, \alpha_i, \alpha_f) = r_0^2 |A_1 + A_2 + A_3 + A_4|^2 \quad (6.16)$$

where r_0 is the classical electron radius, the A_i terms are scattering amplitude corresponding to the four scattering events depicted in fig.6.2 [91], and $q_{||}$ and $q_\perp$ are, respectively, the components of the scattering vector $\mathbf{q}$ in the (x,y) and (x,z) planes defined in fig.6.3

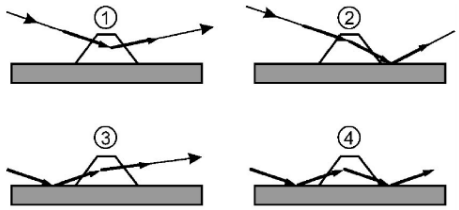

Figure 6.2: *The four scattering events in the DWBA.*

and α_i, α_f are the wave vector incidence and exit angles.

$$A_1(\mathbf{q}_{||}) = \frac{k^2}{4\pi} \int \chi_0(\mathbf{r}) e^{i(q_{||}+q_\perp)\mathbf{r}} dV \quad (6.17)$$

$$A_2(\mathbf{q}_{||}, \alpha_\mathbf{f}) = r(\alpha_f) \frac{k^2}{4\pi} \int \chi_0(\mathbf{r}) e^{i(q_{||}+q_\perp)\mathbf{r}} dV \quad (6.18)$$

$$A_3(\mathbf{q}_{||}, \alpha_\mathbf{i}) = r(\alpha_i) \frac{k^2}{4\pi} \int \chi_0(\mathbf{r}) e^{i(q_{||}+q_\perp)\mathbf{r}} dV \quad (6.19)$$

$$A_4(\mathbf{q}_{||}, \alpha_\mathbf{i}, \alpha_\mathbf{f}) = r(\alpha_i) r(\alpha_f) \frac{k^2}{4\pi} \int \chi_0(\mathbf{r}) e^{i(q_{||}+q_\perp)\mathbf{r}} dV \quad (6.20)$$

Below the critical angle of total external reflection, α_c, the reflection coefficient equals to unity, while the transmission coefficient exhibits a pronounced maximux giving rise to the Yoneda peaks in the diffuse intensity [92].

6.2 GISAXS geometry

A typical GISAXS set up is shown in fig. 6.3. The sample surface defines the (x,y)-plane with the x-axis oriented along the x-ray beam direction. The z-axis is representing the surface normal and as a consequence, the scattering plane is the (x,z)-plane. The incident x-ray beam and the scattered beam are characterized,

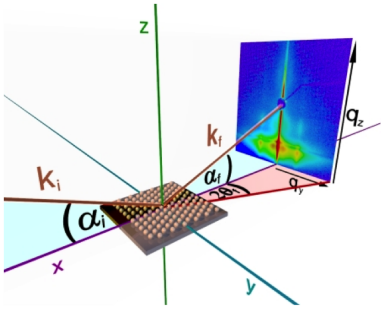

Figure 6.3: *Geometry of a GISAXS experiment. An x-ray beam of wavevector k_i is directed on the sample surface under a grazing incidence angle α_i and is reflected and transmitted by the surface but also scattered along k_f by the surface or subsurface roughness or density heterogeneities.*

respectively, by the wave vector k_i and k_f, that are defined by the in-plane and out-of-plane angles θ_i, α_i, θ_f, and α_f. The specular scattering is achieved when $\alpha_i = \alpha_f$, while diffuse scattering occurs for $\alpha_i \neq \alpha_f$. The momentum transfer q is defined as follow:

$$q = \begin{pmatrix} q_x \\ q_y \\ q_z \end{pmatrix} = \frac{2\pi}{\lambda} \begin{pmatrix} \cos(\alpha_f)\cos(2\theta) - \cos(\alpha_i) \\ \cos(\alpha_f)\sin(2\theta) \\ \sin(\alpha_f) + \sin(\alpha_i) \end{pmatrix} \tag{6.21}$$

In a conventional GISAXS experiment the data are analyzed as a map of $(q_{||}, q_{\perp})$ plane. A typical pattern is made of two main peaks due to the transmitted and specularly reflected beams. The scattering intensity is recorded on a plane, ensuring that the angles are in the range of a few degrees and thus enabling the study of lateral sizes of a few nanometres. Only the upper part of the pattern, $\alpha_f \geq 0$ is accessible because of the shadowing by the substrate surface [93]. At the Yoneda Peaks, the scattering of the sample has its maximum and the exit angle is close to the angle that individuate the total external reflection that is the critical angle, α_c. During a measurement of conventional reflectivity the intensity of reflected beam is measured as a function of the incidence angle, α_i, hence only the q_z vector is involved. The so-obtained pattern is a perpendicular profile of the surface. On the contrary, a GISAXS experiment focuses on the diffuse scattering instead of the specular reflection.

6.3 The unified model

The intensity of the scattered beam is defined by eq.6.22, where $P(q)$ is the form factor, that contains the information about size and shape, and $S(q)$ is the structure factor that describes the spatial arrangement of the objects on the surface and thus their lateral correlations.

$$I(q) = P(q)S(q) \tag{6.22}$$

For a spherical particle island the $P(q)$ function is:

$$P(q) = 4\pi R^3 \frac{\sin(qR) - qR\cos(qR)}{(qR)^3} e^{iq_z R} \tag{6.23}$$

A variation of the incidence angle allows depth profiling of the samples, actually, if the $\alpha_i < \alpha_c$ condition is chosen, the q_z component is zero. As a result, in equation 6.23 the exponential term is the unity. In these conditions the detected volume is that of the deposited nanoobjects, therefore the $P(q)$ becomes the function used routinely in transmission geometry.

In this thesis the model used to fit experimental data is a unified model that takes into account a multi structural level. Beaucage [94] introduced successfully a general unified model in order to take into account several orders of magnitude for spherical averaged particles in transmission scattering geometry using Born approximation. This multilevel approach was applied by Lenz *et al.*, within certain limitations, to analyze scattering problems for multiple structural

levels rather than just one type of scatterer in grazing incidence geometry [95]. This approach allows to model the system's structural features starting from the smallest structural level, such as a nanoparticle towards aggregates of particles. For one structural level the scattered intensity in the unified fit approach is given by eq.6.24 [95]

$$I(q) = Ge^{\frac{-q^2R_g^2}{3}} + B\left(\frac{[erf(qR_g/\sqrt{6}]^3}{q}\right)^P \quad (6.24)$$

The first term corresponds to Guinier's law and describes the size of spherical averaged particles. It is related to the radius of a sphere by the radius of gyration R_g.

$$R_g = \sqrt{\frac{3}{5}}R \quad (6.25)$$

The second term in equation 6.24 corresponds to the structural Porod regime, with the Porod prefactor B, and where P is the slope of this function when plotted on a $\log I$ *vs* $\log q$ plot. When more than one structural level is present in a sample, the unified scattering intensity described in eq.6.24 can be extended to eq.6.26 [94][96]

$$I(q) = \sum_{i=1}^{n} G_i e^{\frac{-q^2R_{g_i}^2}{3}} + B_i e^{\frac{-q^2R_{g_{i-1}}^2}{3}} \left(\frac{[erf(qR_{g_i}/\sqrt{6}]^3}{q}\right)^P \quad (6.26)$$

Equation 6.26 is a sum of scattered intensities over n structural levels. If there are two correlated structural levels, as in aggregates of nanoparticles, a second term, which limits Porod scattering for $n > 1$, at $R_{g_{i-1}}$ has to be introduced.

A traditional interpretation in terms of Guinier and Porod regimes would fail because these are only valid for restricted parts of the q-range; the Guinier method is generally valid only for $qR_g < 1$, while the Porod regime holds at high q-values. These limitations are corrected for in the unified model developed by Beaucage [94]. Furthermore, the traditional methods only account for one level of structural features, whilst the unified model can be extended to account for multiple levels, and therefore it is valid for the entire q-range. The unified model is adapted to analyze the GISAXS patterns of gold samples as Hoell *et al.* have previously developed for thin films [97]: in the eq.6.26 n corresponds to the largest structural level while $i = 1$ corresponds to a smallest structural level than can be observed. If there were any structure at a length scale larger than the n-th level, the corresponding signal would lie outside the q-range covered and hidden by the beamstop, therefore, for the q-range observed here, the unified model was given by the equation:

$$I(q) = G_1 e^{\frac{-q^2R_{g1}^2}{3}} S(q) + G_2 e^{\frac{-q^2R_{g_2}^2}{3}} + + B_2\left(\frac{[erf(qR_{g_2}/\sqrt{6}]^3}{q}\right)^{P_2} + C \quad (6.27)$$

where the numerical subscripts 1 and 2 label the the smaller and the larger structural levels, respectively. The first term, that describes the high-q behaviour (level 1), is a Guinier component with prefactor G_1. R_{g1} is the average radius of gyration; it gives information about the size of the scattering particles at level 1. The Porod term of level 1 is supposed to unmeasurable within the experimental q-range. The second term describes the larger structural level (level 2): the first term within the parentheses is the Guinier term and the last term is the Porod term, with prefactors G_2 and B_2, respectively. R_{g2} is the average radius of gyration; it gives information about the size of the scattering particles at level 2. P_2 is the Porod slope for the same level, giving information about the roughness of the particle surfaces. C is a constant background contribution. In case of weakly correlated

structures the unified intensity can be correlated with a common structure factor

$$I_{corr}(q) = I(q)S(q) \tag{6.28}$$

$S(q)$ describes the correlation between two structures with a centre to centre distance x and a packing factor η.

$$S(q) = \frac{1}{[1 + \eta F(q,x)]} \tag{6.29}$$

The packing factor η outlines the degree of correlation. $F(q,x)$ is the *form factor* for structural correlations occurring at an average distance x and it is given by:

$$F(q,x) = 3\frac{\sin(qx) - qx\cos(qx)}{(qx)^3} \tag{6.30}$$

The previous equations can be used only in the case of weakly correlated systems, when $I(q, R_g)$ can be decoupled from $S(q)$ and $S(q)$ is not dependent on R_g. This is usually the case for low correlations at $\eta < 4$.

6.4 Experimental details

GISAXS experiments were carried out at the beamline BM26 DUBBLE at the ESRF using a sagittal focusing, with a sample-to-detector distance of $1.9m$, a wavelength $\lambda = 0.138nm$, and a beam size of $3217\mu m^2$ (horizontal $\times$ vertical). The critical angle, α_c is found to be equal to $0.175°$, and in order to study the gold nanoparticles supported on the silicon surface, the measurements are performed at $\alpha_i \approx 0.06°$ to keep $\alpha_i < \alpha_c$. The direct and the reflected specular beams are suppressed by small beamstops to prevent damage or saturation of the detector. Instead of the rigorous analysis of the full 2-D detector image, involvingh complex simulations, the global scattering function is used to model transverse detector scans in the reciprocal scattering planes [95]. The 1D-SAXS patterns are obtained from the horizontal cuts of the 2D measurements at the height of the Yoneda peak and are fitted using the unified model [94] described in section 6.3.

6.5 Sample analysis

In fig.6.4 and in fig.6.5 the collected images of the detector are displayed. By inspection of GISAXS pictures, it is possible to notice the presence of a full semicircle instead of annular ring that is typical of nanoparticles with spherical morphology on a flat surface. The amount of vaporized gold onto silicon

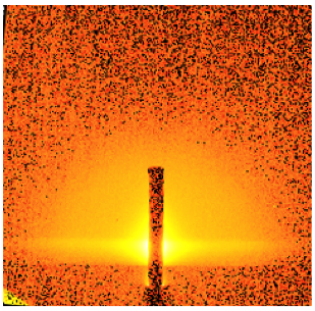

Figure 6.4: *The collected image on the detector for sample Au2*

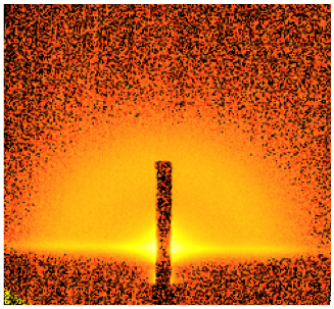

Figure 6.5: *The collected image on the detector for sample Au3*

surface is suitable to obtain a monolayer, therefore the gold nanoparticles would be expected to be organized a monolayer. On the contrary, GISAXS images suggest the presence of high roughness of the samples. Then, two different configurations are supposed: (fig.6.6).

- a gold monolayer grows on highly rough surface:
- gold nanoparticles are organized in a multilayer on a smooth surface.

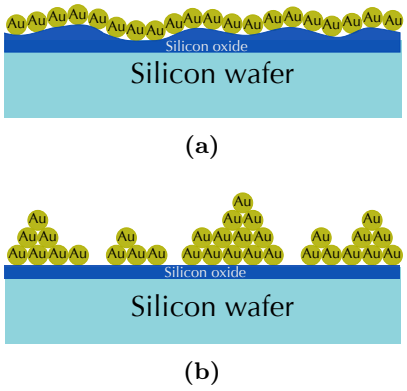

Figure 6.6: *(a) The surface of the wafer exhibits high roughness with an Au nanoparticle monolayer. (b) Gold multilayer deposited on a flat wafer.*

Due to the low value of roughness of silicon surface, detected with AFM measurement, the second possibility is more realistic. Experimental and fitted 1-D data are shown in figs. 6.7-6.8-6.9-6.10. In our experimental q-range, few data-points are recorded, which account for Porod scattering of the level 1. Hence, B_1 is set equal to 0 in the analysis of all the samples. The results obtained from GISAXS analysis are summarized in table 6.1. It is worth noticing that the smaller size values reported in table 6.1, within the error limit, are very similar, suggesting that the mean nanoparticles dimensions are almost the same in all the samples. If

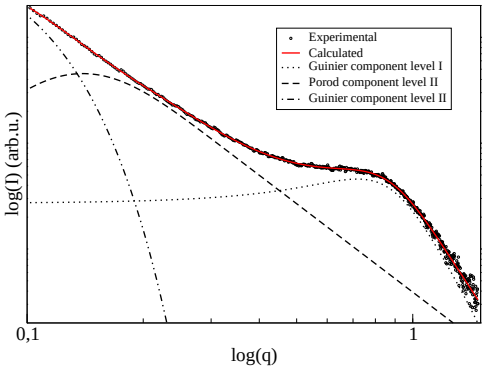

Figure 6.7: *Experimental and fitted GISAXS signal of the Au1 sample. The Porod and Guinier components are also shown.*

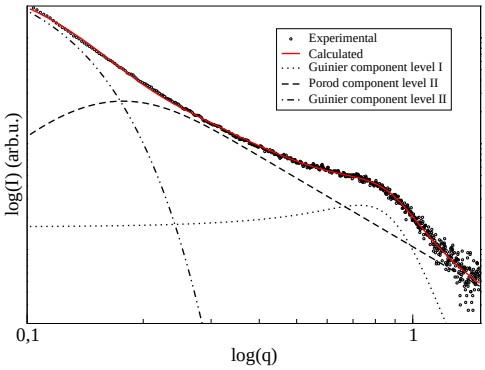

Figure 6.8: *Experimental and fitted GISAXS signal of the Au2 sample. The Porod and Guinier components are also shown.*

we suppose that synthesis method allows to control the size of nanoparticles, this result is not surprising, since the gold nanoparticles are deposited by SMAD technique using the same experimental conditions.

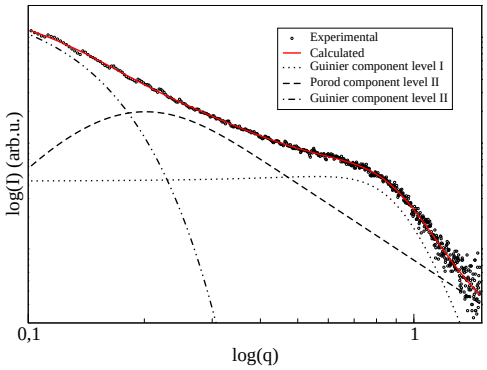

Figure 6.9: *Experimental and fitted GISAXS signal of the Au3 sample. The Porod and Guinier components are also shown.*

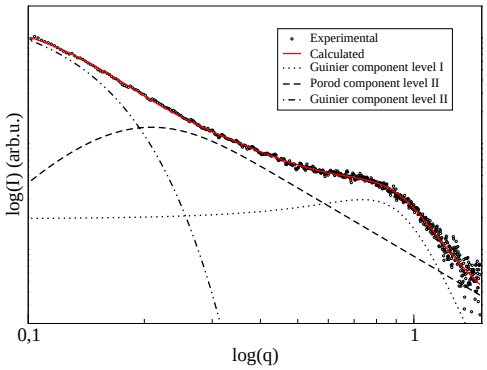

Figure 6.10: *Experimental and fitted GISAXS signal of the Au4 sample. The Porod and Guinier components are also shown.*

The obtained prefactors G_1, as it is shown in table 6.1 are quite different for the analyzed sample, this result is a mere effect of a scaling factor. As what concerns the level 2, then the larger aggregates, the found

Table 6.1: *GISAXS results for the gold samples. The units of the radii are Å, R_1 is the nanoparticle radius, while R_2 is the radius of the aggregates. B_1 is set equal to 0 in the analysis of all the samples.*

	Au1	Au2	Au3	Au4
R_1 (Å)	27	27	27	24
$G_1(10^{-2})$	11.0	0.086	15.0	0.083
η	3.0	4.3	2.4	3.3
R_2 (Å)	216	179	149	144
G_2	7.6	4.7	2.3	1.9
$B_2(10^{-3})$	3.91	10.2	7.84	1.9
P_2	2.78	2.45	2.14	2.14

power law decay of $P_2 \approx 2.5$ can give evidence to a mass fractal, which is related to a three dimensional arrangement of Au primary particles in islands. This result is in agreement with literature data showing that growth of evaporated gold film on a SiO_2/Si surface produces a fractal [98] [99] [100]. For Au film of a thickness of $20nm$ deposited on a Si-substrate grown by thermal evaporation, Lenz *et al.* recently reported a value of $P_2 \approx 1.5$ [95], interpreted as a mass fractal related to a two dimensional arrangement of gold metal nanoparticles. The two Porod parameters are very different. However, this can be ascribed to the different deposition techniques. SMAD synthesis produces three dimensional nanoparticles in an argon atmosphere, whereas in thermal evaporation methods the nanoparticles grow up directly on the surface of the substrate, so the aggregation process of the nanoparticles is totally different [95].

Chapter 7

Discussion

7.1 Silicon supported Au samples

Gold nanocomposites were prepared with an adapted SMAD route. The synthesis protocol involves the vaporization under controlled Argon atmosphere of metallic gold onto a silicon wafer in the presence of the layer of native silicon oxide or of thermal silicon oxide. The low values of the roughness parameter R_q demonstrate the homogeneity of all the investigated gold samples, and whereupon that the SMAD synthesis is a suitable method to obtain a uniform dispersion of gold nanoparticles on a silicon wafer. The structural details of the gold samples were determined at different length scales by AFM, EXAFS and GISAXS. The EXAFS analysis determines much smaller dimensions, in the range of $2-3nm$ (table 3.1), with respect to the AFM result. The Debye-Waller factor of the Au4 sample ($Au/thermal-SiO_2/Si$) is larger than those of the other samples, and considering that a strong correlation between the Debye-Waller factor and coordination number exists, the value of the dimension, in this case might be underestimated. So, the mean cluster dimension of this sample (Au4) could be more similar to those of the other samples. For all samples the EXAFS analysis shows a reduction of the first and second neighbour distance, in agreement with the literature relative to *fcc* gold clusters [101]. An important conclusion of the AFM analysis is that the height of the supported gold nanoparticles depends on the nature of the silicon oxide. Actually, the thermally treated substrate allows to obtain nanoparticles of $9nm$, while the native oxide stabilizes definitely larger aggregates. Focussing the interest on the doped substrates, a smaller dopant concentration involves a larger amount of superficial defects of the native silicon oxide layer: taking into account that the surface defects act as nucleation centers [83], it seems feasible to conclude that the gold nanoclusters give rise to larger aggregates on a surface poor of defects. On the contrary, at increasing dopant concentration the metal clusters aggregate in small units. However, the large discrepancy between the EXAFS and the AFM result is clearly relative to two different length scales: with this respect, the GISAXS analysis is very useful to elucidate the supported Au morphology: from the GISAXS analysis, we found two different sizes, the smaller, that is the nanocluster radius, is in agreement

to the EXAFS analysis, while the larger can be related to the radius of the aggregates. A detailed analysis of the AFM images put in evidence that the aggregates could be made up of several smaller particles, so that the smaller gold clusters of $2-3nm$ in radius constitute the building blocks of the larger structures detected in the GISAXS patterns and AFM images. It is interesting to notice that the size of the larger objects detected by GISAXS decreases with increasing dopant level in the silicon substrate, in agreement to AFM analysis.

7.2 Unsupported Co samples

Unsupported Co samples were prepared by thermal decomposition putting a metal precursor, $Co_2(CO)_8$, in an organic solvent in presence of octadecylamine. TEM measurements show the nanometer size of so obtained powder samples. The EXAFS analysis demonstrate that both hexagonal and cubic sequences of atomic layers are required to obtain satisfactory fits of the experimental spectra. This result is in agreement with the XRD analysis as concern the phase amounts, within the errors on the determination of the percentages of *hcp* and *fcc* sequences from the EXAFS data. From the HRXRD analysis the sample with the highest *fcc* component is D15, that is prepared with mesytilene as solvent. Since the hexagonal arrangement is the most stable at room temperature, in D15 the high amount of cubic arrangement is probably due to the higher synthesis temperature. Indeed, the D3 and D4 samples, that were prepared with heptane, a solvent with a boiling temperature lower than mesytilene, show a larger amount of hexagonal sequences with respect to D15. The capping agent has no effect about the arrangement, but avoids particle coalescence in all the samples, as it is demonstrated by TEM and HRXRD analysis. The three investigated samples have similar average size, as results from the HRXRD analysis, while the percentage of *hcp* and *fcc* sequences are very different: it is likely to conclude that with a suitable choice of the solvent it it possible to modulate the amount of *hcp* and *fcc*, keeping the same nanometer size of particles.

7.3 Silicon supported Co samples

The cobalt nanocomposites were prepared with an adapted SMAD route. The synthesis involves the vaporization of cobalt under a controlled Argon atmosphere and deposition onto a silicon wafer in the presence of the layer of native silicon oxide. As for gold nanoparticles deposition, the SMAD technique is suitable to obtain homogeneous dispersion of the cobalt nanoclusters on the silicon wafer, as it is demonstrated by the low calculated roughness from the collected AFM images. The measurement of the XRD pattern of nanosized cobalt deposited onto a surface requires a grazing incidence geometry, that is hardly available with laboratory instrumentation and is feasible, at synchrotron radiation facilities, only at dedicated beamlines. During my Ph.D. work, the relative amounts of the cubic and hexagonal arrangements could only be determined by EXAFS analysis. Although the EXAFS analysis is less suitable than XRD for a thorough analysis of stacking faults, the EXAFS result, pointing to a substantial independence of this disorder from the exploited solvent and capping agent, seems reliable, taking into account that the interaction of the cobalt particles with the surface of the silicon wafer is likely the dominant effect.

With respect to Cobalt foil, (see table 3.7) it is possible to notice a reduction of the first neighbour

distance R_1 for the cubic arrangement and an expansion for the *hcp* arrangement. The size of supported Co nanoparticles, as determined by EXAFS and AFM, is very different, likely due to a higher resolution of the scattering technique, able to resolve at a smaller length scale the structure of the aggregates. At this length scale, it seems that the presence of the capping agents does not influence the particle size (3.7). On the other hand, (see fig. .5.7 and table 5.3) the AFM analysis evidences a definite difference of the height distribution function of the ODA samples with respect to the other Co samples. In particular, it can be concluded that the ODA capping is able to prevent nanoparticle aggregation. With this respect, the use of capping agents seems a valid tool to enhance the control on morphology. From the AFM analysis, also the solvent effect can be identified, most clearly when the capping agent is missing. Actually, it can be noticed from the height function distribution (fig.5.7) that the peak maximum has different values for the three solvent, pointing to a different interaction of the three solvents with the cobalt nanoparticles. In fact, mesitylene and toluene, both containing an aromatic group, are able to better prevent the coalescence, and allow to obtain a lower particle size than heptane. The cobalt oxide shells are evident in the Fourier Transform of the EXAFS spectra of Co tol and Co tol ODA sample. The high solubility of toluene in water can explain the oxidation of these nanocluster, since the presence of water promotes the oxidation of metallic cobalt. Actually, toluene, even if just distilled, absorbs water, and in fact its solubility in distilled water is 543 ppm at 300K [102]. On the contrary, at room temperature mesytilene is totally insoluble in distilled water, and the EXAFS data of Co mes show a much lower oxide component that is totally absent in the Co mes ODA sample. The magnetic domains of the samples with the highest amount of metallic component were investigated with MFM. The MFM of Co mes ODA sample shows a larger magnetic contrast with respect to Co ept, probably due to lower coercivity of the latter.

Chapter 8

Conclusion and perspectives

8.1 Conclusion

In this thesis cobalt nanoparticles and supported cobalt and gold nanoparticles have been synthesized and investigated, using a number of techniques, to study their structure and their morphology. The prepared nanocomposites show nanoparticles organized in aggregates supported on silicon surface. The control of size for gold aggregates is achieved as a function of silicon doping and, for cobalt aggregates, as a function of a capping agent. Between the tested capping agent the ODA (octadecylamine) avoids the coalescence but has no effects on the crystalline structure. This result is limited to this molecule, with other agents (TOA) that yield an high amount of oxide phase it is impossible to obtain robust result as concern the crystalline arrangement and stacking faults. Though a fine control on arrangement is not reached, an effect due to the solvent on the sequences of layer is identified. The solvent, mesytilene, with the higher boiling temperature, that is also the synthesis temperature, yields an high amount of cubic arrangement percentage, that is, traditionally, the less stable at room temperature. The temperature of nanoparticles preparation would be supposed to influence the arrangement, the implication is that lower synthesis temperature would give rise to the most stable arrangement, *hcp*, while the higher temperature would provide the cubic phase. The water solubility in the reaction solvent explain why the mesytilene is also able to keep the metallic state of cobalt avoiding the oxidation, while the toluene occurs the oxidation of cobalt.

8.2 Perspectives

Tailoring the amount of hexagonal and cubic sequences of metallic cobalt and the oxide amount, devices with sought-after magnetic properties can be designed. The planning of synthesis routes to obtain Co and Au nanocomposites with controlled morphology is a work in progress, requiring further investigation on synthesis parameters, solvents and capping agents to improve the knowledge obtained during this Ph.D. work.

Further studies will involve also the possibility of obtaining new morphologies, such as the worm-like Au particles shown in fig.8.1-8.2. To my knowledge, this kind of morphology is absolutely new for metal

aggregates. Actually, the achievement of this kind of superstructures is due to a lucky event; the production of the worm-like systems is accounted for the presence of the siliconic oils that could came from the rotative oil vacuum pump. The hypothesis is that this oil can act as capping agent addressing the growth of the aggregates towards a worm-like shape. The employment of the Atomic Force Microscopy was crucial to detect the morphology of these aggregates, because it is impossible to determine a worm-like aggregation with other techniques. The worm-like aggregates constitute a first result of new synthesis procedures aiming to the growth of aggregates with specific morphology in order to pattern silicon surface. The well-known covalent bond between gold and sulphur should allow to functionalize a gold worm-like structure with aliphatic thiols to obtain a surface with hydrophilic and hydrophobic domains.

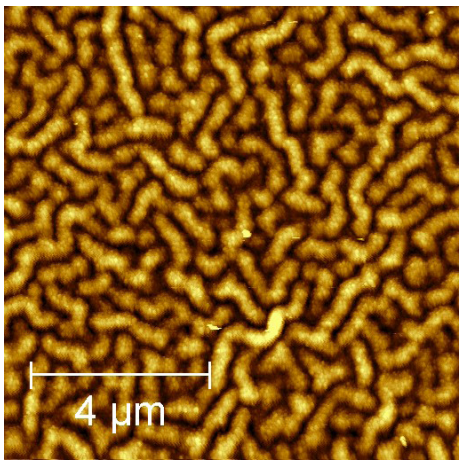

Figure 8.1: *AFM image* $4\mu m x 4\mu m$ *of a* worm-like *gold sample.*

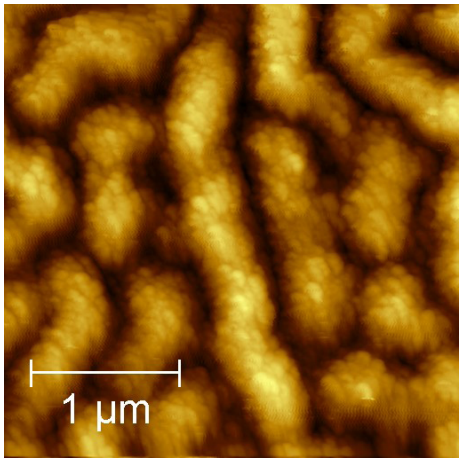

Figure 8.2: *AFM image* $1\mu m x 1\mu m$ *of a* worm-like *gold sample.*

References

[1] E. Roduner, *Chem. Soc. Rev.* **35**, 583 (2006).

[2] M. Attarian Shandiz, *J. Phys.; Condens. Matter.* **20**, 325237 (2008).

[3] M. Attarian Shandiz and A. Safaei, *Materials Letters* **62**, 3954 (2008).

[4] G. Bond and D. Thompson, *Appl. Catal. A* **302**, 1 (2006).

[5] Y. Lei, F. Mehmood, S. Lee, J. Greeley, B. Lee, S. Seifert, R. E. Winans, J. W. Elam, R. J. Meyer, P. Redfern, D. Teschner, R. Schlogl, M. J. Pellin, L. A. Curtiss, and S. Vajda, *Science* **328**, 224 (2010).

[6] N. Rosi and C. Mirkin, *Chem. Rev* **105**, 1547 (2005).

[7] P. Gambardella, S. Rusponi, M. Veronese, S. Dhesi, C. Grazioli, A. Dallmeyer, I. Cabria, R. Zeller, K. Dederichs, P.H. Kern, C. Carbone, and H. Brune, *Science* **300**, 1130 (2003).

[8] M. Haruta, T. Kobayashi, H. Samo, and Y. N., *Chemistry Letters* **2**, 405 (1987).

[9] M. Haruta, N. Yamada, T. Kobayashi, and S. Iijima, *Journal of Catalysis* **115**, 301 (1989).

[10] M. Haruta, S. Tsubota, T. Kobayashi, H. Kageyama, M. Genet, and B. Delmon, *Journal of Catalysis* **144**, 175 (1993).

[11] A. Venezia, G. Pantaleo, A. Longo, G. Di Carlo, M. Casaletto, L. Liotta, and G. Deganello, *J. Phys. Chem. B* **109**, 2821 (2005).

[12] A. Prestianni, A. Martorana, F. Labat, I. Ciofini, and C. Adamo, *Journal of Physical Chemistry B* **110**, 12240 (2006).

[13] B. Johannessen, P. Kluth, C. Glover, G. Foran, and M. Ridgway, *Nucl. Instrum. Meth. B* **242**, 133 (2006).

[14] K. Jung, J. Yoon, N. Koshizaki, and Y. Kwon, *Curr. Appl. Phys.* **8**, 761 (2008).

[15] D. Yang, E. Sacher, and M. Meunier, *Appl. Phys. A* **80**, 575 (2005).

[16] D. Yang, E. Sacher, and M. Meunier, *Appl. Phys. A* **80**, 575 (2005).

[17] H. Nam, T. Sasaki, and N. Koshizaki, *J. Phys. Chem. B* **110**, 23081 (2006).

[18] Z. Chen, J. Jie, L. Luo, H. Wang, C. Lee, and S. Lee, *Nanotechnology* **18**, 345502 (2007).

[19] L. Guczi, G. Peto, K. Beck, A. Frey, O. Geszti, G. Molna, and C. Daroczi, *J. Am. Chem. Soc.* **125**, 4332 (2003).

[20] J. Carter, Y. Qu, R. Porter, L. Hoang, D. Masiel, and T. Guo, *Chem. Commun.* , 2274 (2005).

[21] C. Hu, T. Chang, C. Tu, P. Shueh, C. Lin, S. Sze, T. Tseng, and M. Chen, *Applied Physics Letters* **94**, 102106 (2009).

[22] M. Daniel and D. Astruc, *Chemical Review* **104**, 293 (2004).

[23] G. Deganello, F. Giannici, A. Martorana, G. Pantaleo, A. Prestianni, A. Balerna, L. F. Liotta, and A. Longo, *J. Phys. Chem. B* **110**, 8731 (2006).

[24] F. Ruffino, M. G. G. F. B. C. Canino, A.and Grimaldi, F. Roccaforte, and V. Raineri, *J. Appl. Phys.* **101**, 064306 (2007).

[25] C. M. Niemeyer, *Angew. Chem. Int. Ed.* **40**, 4128 (2001).

[26] A. Longo and A. Martorana, *J. Appl. Cryst* **41**, 446 (2008).

[27] Q. Fu, H. Saltsburg, and M. Flytzani-Stephanopoulos, *Science* **301**, 935 (2003).

[28] U. Heiz and W. Schneider, *J. Phys. D Appl. Phys.* **31**, R85 (2000).

[29] J. Guzman and B. Gates, *J. Phys. Chem. B* **106**, 7659 (2002).

[30] S. H. Overbury, L. Ortiz-Soto, H. Zhu, B. Lee, M. D. Amiridis, and S. Dai, *Catal. Lett.* **95**, 99 (2004).

[31] B. Chithrani, A. Ghazani, and W. Chan, *Nanoletters* **6**, 662 (2006).

[32] J. Garcia-Serrano, A. Galindo, and U. Pal, *Sol. Energy Mater. Sol. Cell* **82**, 291 (2004).

[33] U. Pal, E. Aguila Almanza, O. Vazquez Cuchillo, N. Koshizaki, T. Sasaki, and S. Terauchi.

[34] H. Jun, K. Lee, S. Yoon, T. Lee, I. Kim, J. Jeong, B. Cheong, D. Kim, K. Cho, and W. Kim, *Phys. Stat. Sol. a* **203**, 1211 (2006).

[35] J. Xu and C. Perry, *J.Non-Cryst. Solids* **353**, 1212 (2007).

[36] H. Ko, M. Mizuhata, A. Kajinami, and S. Deki, *Thin Solid Films* **491**, 86 (2005).

[37] v. Su, M. Li, Z. Zhou, Y. Zhai, Q. Fu, C. Huang, and Z. Song, H. Hao, *J. Lumin.* **128**, 642 (2008).

[38] D. Kim, E. Koyama, H. Tokuhisa, N. Koshizaki, and Y. Kim, *Appl. Phys. A* **92**, 263 (2008).

[39] W. Betteridge, *Prog. Mater. Sci* **24**, 51 (1979).

[40] A. Wilson, *Proceeding of the Royal Society* **180**, 277 (1941).

[41] W. Sucksmith and J. Thompson, *Proc. R. Soc. Lond. A* **225**, 362 (1954).

[42] J. Coey, *Magnetism and magnetic materials*, Cambridge University Press: New York, 2010.

[43] J. Sort, S. Surinach, J. Munoz, M. Baro, E. Jedryka, S. Nadolski, N. Sheludko, and J. Nogues, *Phys. Rev. B.* **68**, 014421 (2003).

[44] R. Speight, A. Wong, P. Ellis, P. Bishop, T. Hyde, T. Bastow, and M. Smith, *Phys. Rev. B.* **79**, 054102 (2009).

[45] C. Maurizio, G. Mattei, P. Canton, E. Cattaruzza, C. de Julian Fernandez, P. Mazzoldi, F. D'Acapito, G. Battaglin, C. Scian, and A. Vomiero, *Materials Science and Engineering* **27**, 193 (2007).

[46] N. Rosengaard and H. Skriver, *Physical Review B* **47**, 1858 (1993).

[47] K. Manninen and M. Manninen, *The European Physical Journal D* **20**, 243 (2002).

[48] J. Cai, F. Wang, C. Lu, and Y. Wang, *Physical Review B* **69**, 224104 (2004).

[49] S. Moudikoudis, K. Simeonidis, A. Vilalta-Clemente, F. Tuna, I. Tsiaoussis, M. Angelakeris, C. Dendrinou-Samara, and O. Kalogirou, *Journal of Magnetism and Magnetic Materials* **321**, 2723 (2009).

[50] G. Liu, X. Yan, Z. Lu, S. Curda, and L. J., *Chem. Mater.* **17**, 4985 (2005).

[51] Y. Mi, D. Yuan, Y. Liu, J. Zhang, and Y. Xiao, *Materials Chemistry and Physics* **89**, 359 (2005).

[52] R. de Silva, V. Palshin, K. de Silva, L. Henry, and C. Kumar, *J. Mater. Chem.* **18**, 738 (2008).

[53] A. Zolotaryov, Y. Bugayev, V. Samifalov, O. Devizenko, E. Zubarev, S. Martens, and O. Albrecht, *Physica Status Solidi a* (2011).

[54] V. Skumryev, S. Stoyanov, Y. Zhang, G. Hadjipanayis, D. Givord, and J. Nogues, *Nature* **423**, 850 (2003).

[55] H. Hori, T. Teranishi, Y. Nakae, Y. Seino, M. Miyake, and S. Yamada, *Phys. Lett. A* **263**, 406 (1999).

[56] Y. Yamamoto, T. Miura, M. Suzuki, N. Kawamura, H. Miyagawa, T. Nakamura, K. Kobayashi, T. Teranishi, and H. Hori, *Physical Review Letters* **93**, 116801 (2004).

[57] S. Pundlik, K. Kalyanaraman, and U. Waghmare.

[58] V. Raffa, B. Mazzolai, A. Mondini, V. Mattoli, A. Menciassi, and P. Dario, *Sensor and Actuators B* **122**, 475 (2007).

[59] A. Lagunas, C. Jimeno, D. Font, L. Sola, and M. Pericas, *Langmuir* **22**, 3823 (2006).

[60] V. Puntes, K. Krishnan, and A. Alivisatos, *Science* **291**, 2115 (2001).

[61] K. Klabunde, *Free Atoms Clusters, and Nanoscale Particles*, Academic press, 1994.

[62] S. Stoeva, L. Prasad, S. Uma, P. Stoimenov, V. Zaikovski, C. Sorensen, and K. Klabunde, *Journal of Physical Chemistry B* **107**, 7441 (2003).

[63] G. Koretsky, K. Kerns, G. Nieman, M. Knickelbein, and S. Riley, *J. Phys. Chem. A* **103**, 1997 (1999).

[64] X. Zhang, *Electrochemistry of Silicon and its oxide*, New York. Kluwer Academic/Plenum Publishers, 2001.

[65] B. Teo, *EXAFS: basic principles and data analysis*, Springer-Verlag, 1986.

[66] G. Bunker, *Introduction to XAFS: a pratical guide to X-ray Absorption Fine Structure Spectroscopy*, Cambridge University press, 2010.

[67] M. Newville, *J. Synchrotron Rad.* **8**, 322 (2001).

[68] B. Ravel and M. Newville, *J. Synchrotron Rad.* **12**, 537 (2005).

[69] A. Filipponi and A. Di Cicco, *Phys. Rev.B* **52**, 15135 (1995).

[70] M. Borowski, *J. Phys. IV* **7**, C2 (1997).

[71] J. Kakinoki and T. Komura.

[72] J. Kakinoki.

[73] G. Binnig and H. Rohrer, *IBM Journal of Research and Development* **30** (1986).

[74] G. Binnig, H. Rohrer, C. Gerber, and E. Weibel, *Applied Physics Letters* **40**, 178 (1982).

[75] G. Binnig, C. F. Quate, and C. Gerber, *Phys. Rev. Lett.* **56**, 930 (1986).

[76] P. Eaton and P. West, *Atomic force microscopy*, Oxford University Press, 2010.

[77] Y. Martin, C. C. Williams, and H. K. Wickramasinghe, *Journal of Applied Physics* **61**, 4723 (1987).

[78] Y. Martin and H. K. Wickramasinghe, *Applied Physics Letters* **50**, 1455 (1987).

[79] P. Klapetek, D. Necas, and C. Anderson, Gwyddion user guide, `http://gwyddion.net/`, 2004–2009.

[80] Y. Ishimaru, M. Yoshiki, and T. Hatanaka, *Mater. Res. Soc. Symp. Soc. Proc.* **259**, 405 (1992).

[81] A. Wolkenberg, *Physica Status Solidi A* **79**, 313 (1983).

[82] X. Zhang, *Electrochemistry of silicon and its oxide*, Kluwer Academic Publishers, 2001.

[83] A. Del Vitto, G. Pacchioni, K. H. Lim, N. Rosch, J. Antonietti, M. Michalski, U. Heiz, and H. Jones, *J. Phys. Chem. B* **109**, 19876 (2005).

[84] X. Cai, P. Zhang, L. Ma, W. Zhang, X. Ning, L. Zhao, and J. Zhuang, *J. Phys. Chem. A* **113**, 4889 (2009).

[85] J. Antonietti, M. Michalski, U. Heiz, H. Jones, K. Lim, A. Rosch, N. Del Vitto, and G. Pacchioni, *Phys. Rev. Lett.* **94**, 213402 (2005).

[86] M. Munford, L. Seligman, M. Sartorelli, E. Voltolini, L. MArtins, W. Schwarzacher, and P. A.A., *Journal of Magnetism and Magnetic Materials* **226-230**, 1613 (2001).

[87] J. Daillant and A. Gibaud, *X-ray and neutron reflectivity: principles and applications*, Springer, 2009.

[88] S. Sinha, E. Sirota, S. Garoff, and H. Stanley, *Physical Review B* **38**, 4 (1988).

[89] G. Vineyard, *Phys.Rev.B.* .

[90] K. Stoev and K. Sakurai, *The Rigaku Journal* **14**, 22 (1997).

[91] M. Schmidbauer, D. Grigoriev, M. Hanke, P. Schafer, T. Wiebach, and R. Kohler, *Physical review B* **71**, 115324 (2005).

[92] Y. Yoneda, *Phys. Rev. B* **131**, 2010 (1963).

[93] R. Lazzari, *Journal of Applied Crystallography* **35**, 406 (2002).

[94] G. Beaucage, *Journal of Applied Crystallography* **28**, 717 (1995).

[95] S. Lenz, M. Bonini, S. Nett, M. Lechmann, S. Emmerling, R. Kappes, M. Memesa, A. Timmann, S. Roth, and J. Gutmann, *The European Physical Journal Applied Physics* **51**, 10601 (2010).

[96] K. Kravchyk, Y. Gomza, O. Pashkova, O. V'yunov, S. Nesin, and A. Belous, *Journal of Non-Crystalline Solids* **355**, 2557 (2009).

[97] K. Hoydalsvik, T. Barnardo, R. Winter, S. Haas, D. Tatchev, and A. Hoell, *Phys. Chem. Chem. Phys.* **12**, 14492 (2010).

[98] L. Vazquez, R. Salvarezza, P. Herrasti, P. Ocon, J. Vara, and J. Arvia, *Surface Science* **345**, 17 (1996).

[99] M. Aguilar, E. Anguiano, J. Aznarez, and J. Sacedon, *Surface Science* **482-485**, 935 (2001).

[100] S. Jurecka, H. Kobayashi, M. Takahashi, T. Matsumoto, M. Jureckova, F. Chovanec, and E. Pincik, *Applied Surface Science* **256**, 5623 (2010).

[101] A. Balerna, E. Bernieri, A. Picozzi, P. Reale, S. Santucci, E. Burattini, and S. Mobilio, *Phys. Rev. B* **31**, 5058 (1985).

[102] C. Sutton and J. Calder, *Journal of Chemical and Engineering Data* **20**, 320 (1975).

Appendix A

TEM images

The particle size and the morphology of the samples were determined by TEM measurements collected at the IMM-CNR of Bologna. The powders were dispersed in isopropanol and mildly sonicated, then drop-casted on a standard TEM grid for the observations. The samples present particle aggregates of micron size, with nanoparticles of few nanometers of about of 2-6 nm diameter.

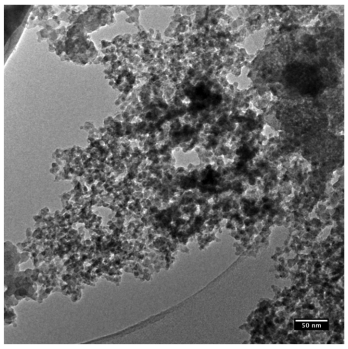

(a)

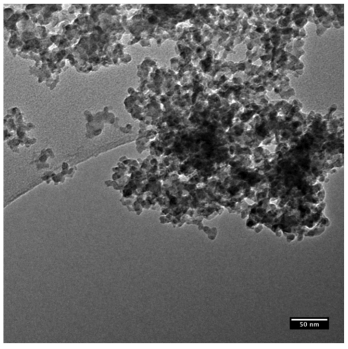

(b)

Figure A.1: *TEM of D3 sample.*

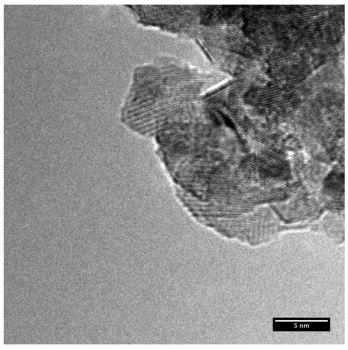

(a)

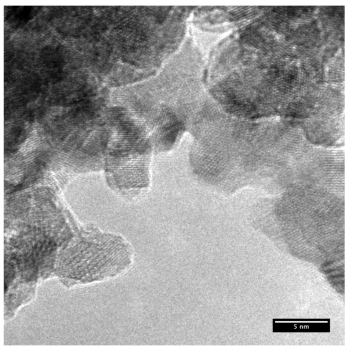

(b)

Figure A.2: *HrTEM of D3 sample.*

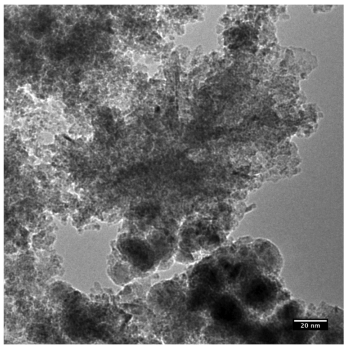

(a)

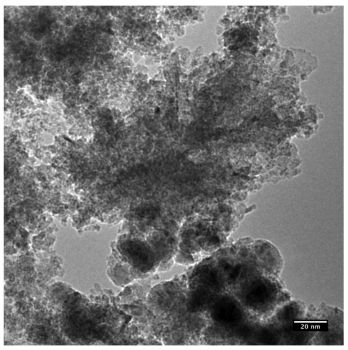

(b)

Figure A.3: *TEM of D15 sample.*

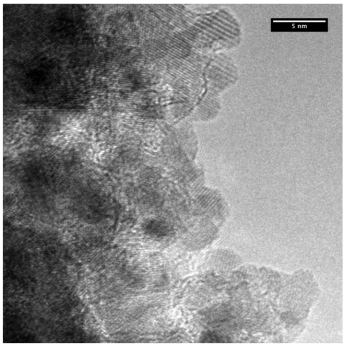

(a)

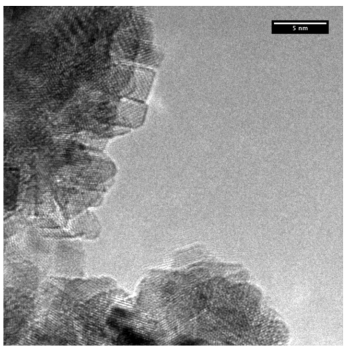

(b)

Figure A.4: *HrTEM of D15 sample.*

Appendix B

AFM image

The AFM images are measured at the ISMN (Istituto dei Materiali Nanostrutturati) of the CNR of Bologna. Here all images are collected to make fluent the reading. From fig.B.16 to fig.B.19 are inserted the 3D images of the gold nanoparticles deposited on silicon wafer whose surface is covered with native oxide except one case, the Au4 sample, that exhibit an oxide grown up thermally before the metal vaporization. The thickness of the thermal oxide of the Au4 sample is 591nm. The images $5\mu n$x$5\mu n$, $3\mu n$x$3\mu n$, and $1\mu n$x$1\mu n$ of cobalt nanoparticles supported on silicon wafer are shown from fig.B.1 to B.15. All nanocobalt supported samples are prepared using silicon wafer with native oxide.

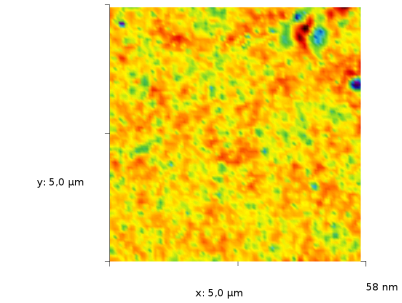

(a)

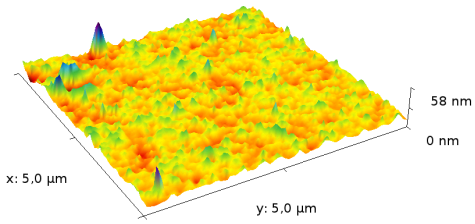

(b)

Figure B.1: *AFM $5\mu m$x$5\mu m$ of the Co mes ODA sample. (a) 2D image (b) 3D image.*

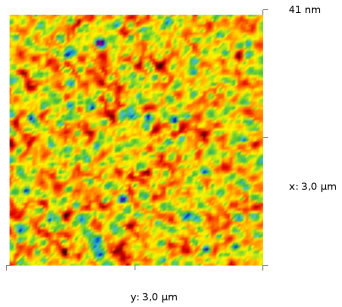

(a)

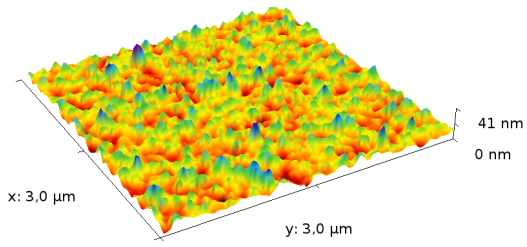

(b)

Figure B.2: *AFM* $3\mu m x 3\mu m$ *of the Co mes ODA sample. (a) 2D image (b) 3D image.*

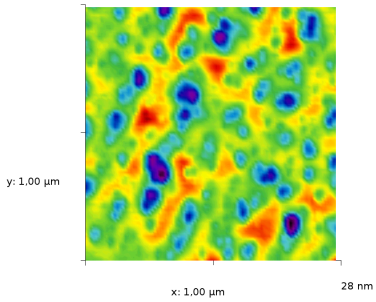

(a)

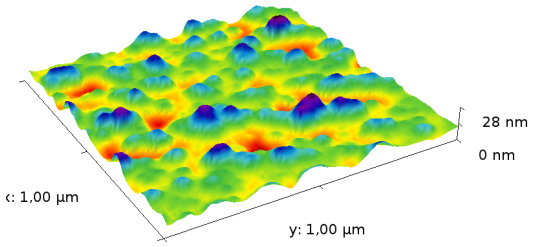

(b)

Figure B.3: *AFM* $1\mu m x 1\mu m$ *of the Co mes ODA sample. (a) 2D image (b) 3D image.*

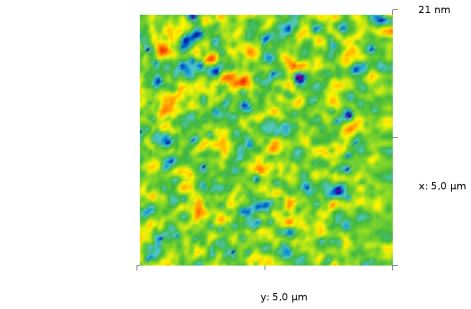

(a)

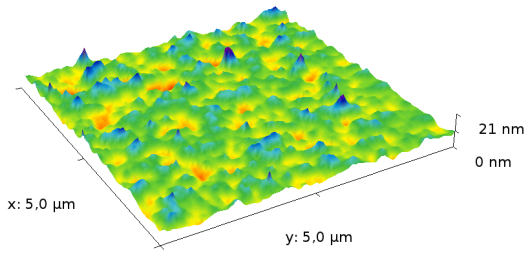

(b)

Figure B.4: *AFM 5µmx5µm of the Co mes sample. (a) 2D image (b) 3D image.*

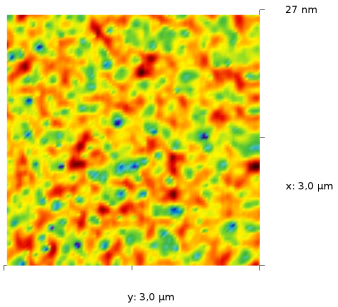

h

(a)

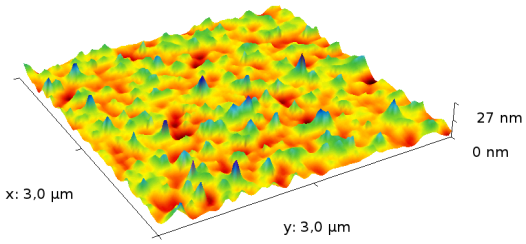

(b)

Figure B.5: *AFM 3µmx3µm of the Co mes sample. (a) 2D image (b) 3D image.*

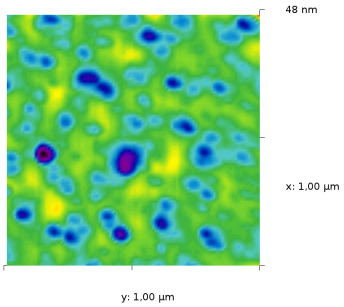

(a)

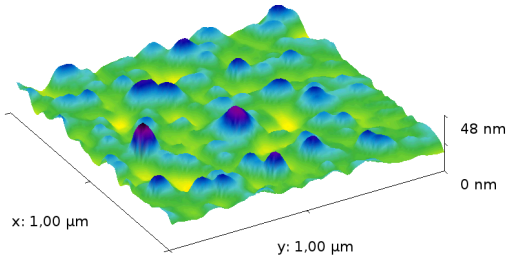

(b)

Figure B.6: *AFM* $1\mu m x 1\mu m$ *of the Co mes sample. (a) 2D image (b) 3D image.*

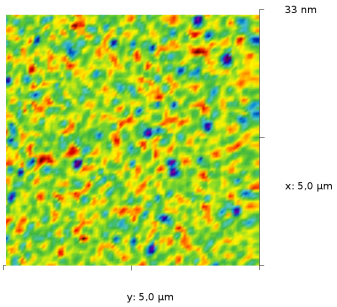

(a)

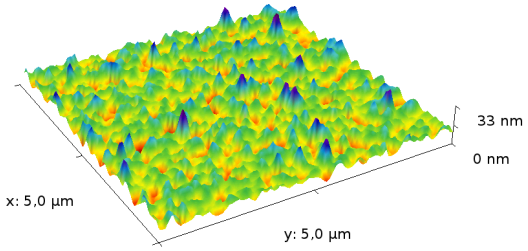

(b)

Figure B.7: *AFM* $5\mu m x 5\mu m$ *of the Co tol ODA sample. (a) 2D image (b) 3D image.*

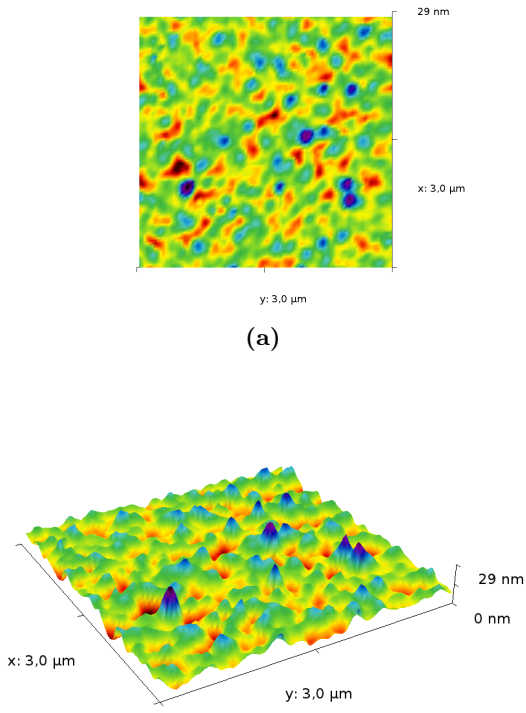

(a)

(b)

Figure B.8: *AFM 3μmx3μm of the Co tol ODA sample. (a) 2D image (b) 3D image.*

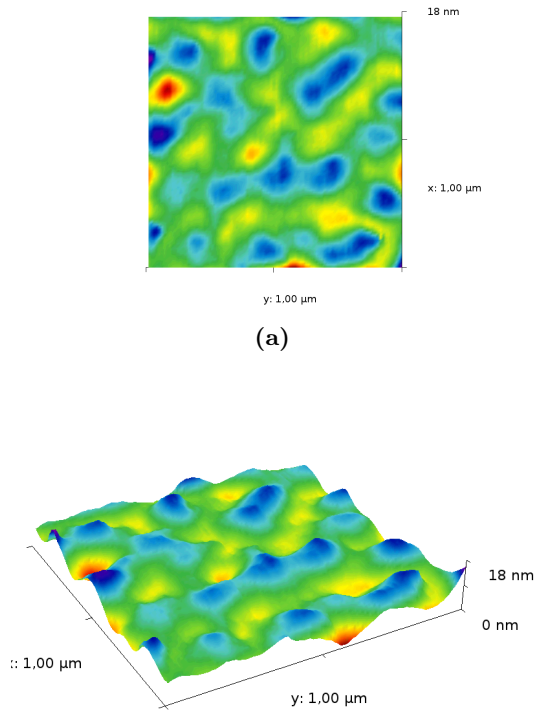

(a)

(b)

Figure B.9: *AFM 1μmx1μm of the Co tol ODA sample. (a) 2D image (b) 3D image.*

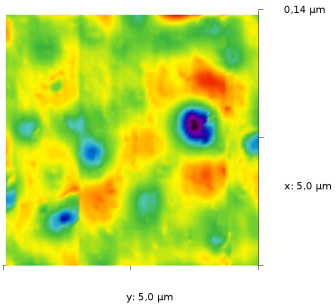

(a)

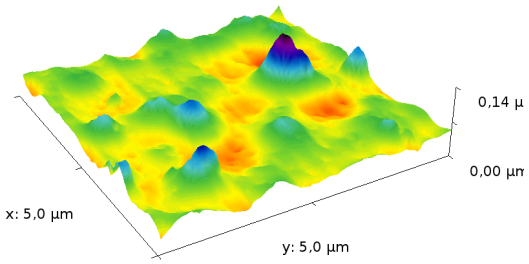

(b)

Figure B.10: *AFM 5μmx5μm of the Co tol sample. (a) 2D image (b) 3D image.*

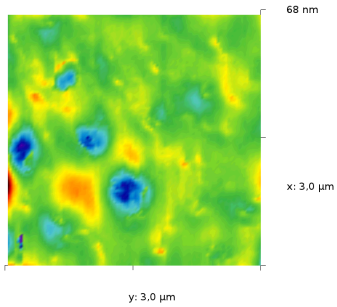

(a)

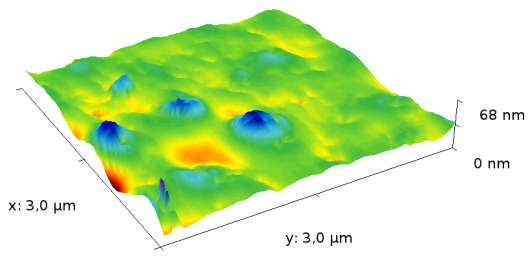

(b)

Figure B.11: *AFM 3μmx3μm of the Co tol sample. (a) 2D image (b) 3D image.*

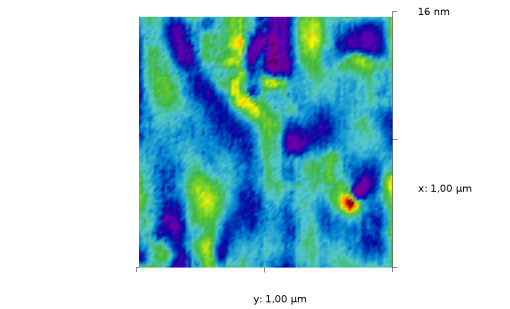

(a)

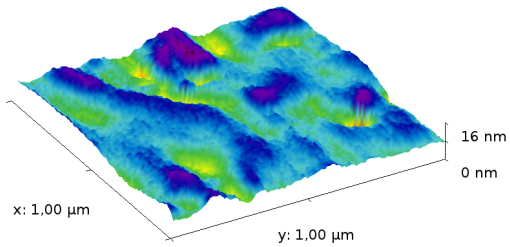

(b)

Figure B.12: *AFM* $1\mu m x 1\mu m$ *of the Co tol sample. (a) 2D image (b) 3D image.*

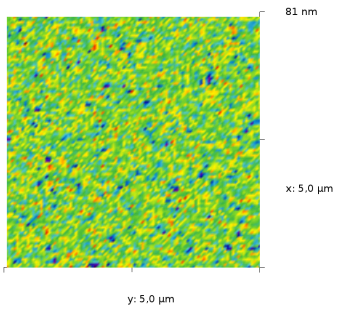

(a)

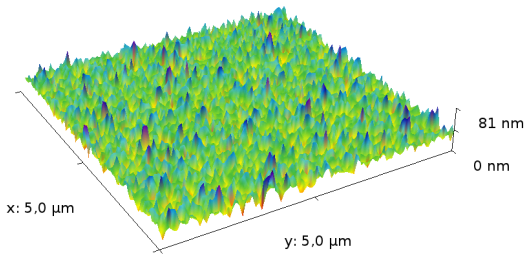

(b)

Figure B.13: *AFM* $5\mu m x 5\mu m$ *of the Co ept sample. (a) 2D image (b) 3D image.*

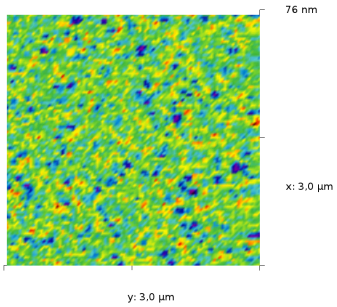

(a)

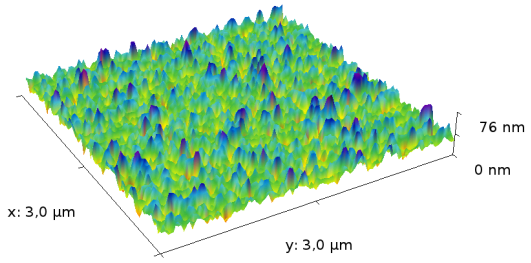

(b)

Figure B.14: *AFM* $3\mu m x 3\mu m$ *of the Co ept sample. (a) 2D image (b) 3D image.*

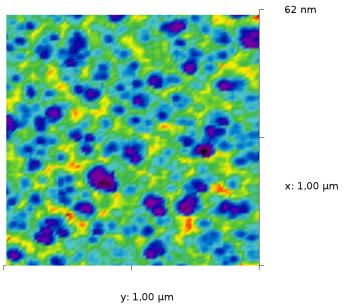

(a)

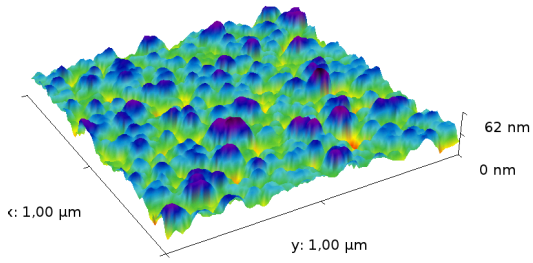

(b)

Figure B.15: *AFM* $1\mu m x 1\mu m$ *of the Co ept sample. (a) 2D image (b) 3D image.*

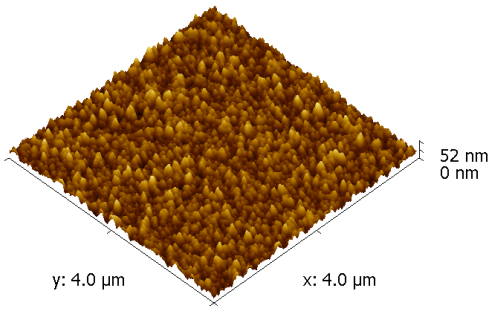

Figure B.16: *AFM* $4\mu m x 4\mu m$ *of the Au1 sample.*

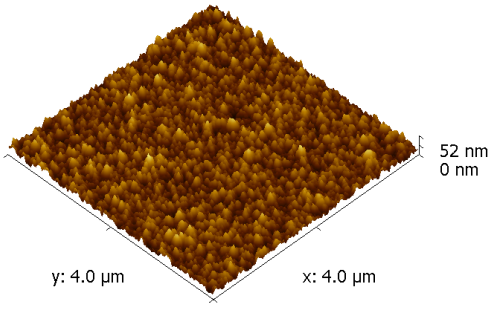

Figure B.18: *AFM* $4\mu m x 4\mu m$ *of the Au3 sample.*

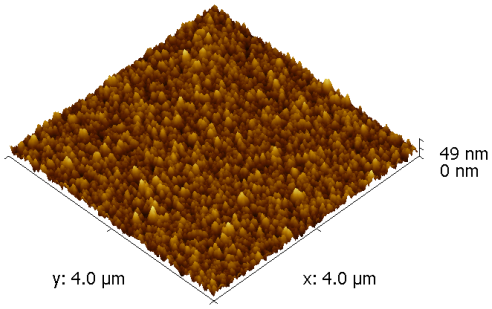

Figure B.17: *AFM* $4\mu m x 4\mu m$ *of the Au2 sample.*

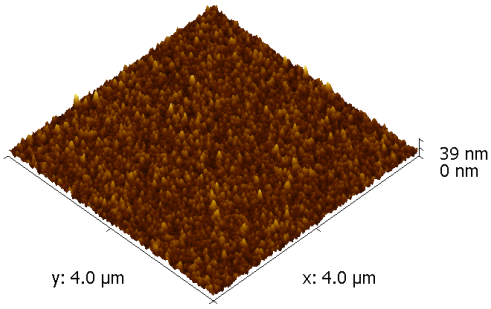

Figure B.19: *AFM* $4\mu m x 4\mu m$ *of the Au4 sample.*

Appendix C

Curriculum vitae

Publications

- L. Sciortino, F. Giannici, A. Martorana, A. Ruggirello, V. Turco Liveri, G. Portale, M. P. Casaletto, and A. Longo. "Structural Characterization of Surfactant-Coated Bimetallic Cobalt/Nickel Nanoclusters by XPS, EXAFS, WAXS, and SAXS" *J. Phys. Chem. C*, 2011, 115, 6360-6366;

- L. Sciortino, A. Longo, F. Giannici, A. Martorana. " Effect of the capping agents on cobalt nanoparticles" *Journal of Physics: Conference Series*, 2009, 190, 012125;

- F. Giannici, D. Messana, A. Longo, L. Sciortino and A. Martorana. "Local structure of gallate proton conductors" *Journal of Physics: Conference Series*, 2009, 190, 012077.

Publications in preparation

- L. Sciortino, A. Longo and A. Martorana, "New approch to analyze distrorted *hcp* metal clusters: an XRD and EXAFS study";

- G. Portale, L. Sciortino, F. Giannici, A. Martorana, C. Albonetti, F. Biscarini, A. Longo "Gold clusters deposited on the native silica oxide: EXAFS, GISAXS and AFM study";

- L. Sciortino, A.M. Ruggirello, A. Balerna, A. Martorana, V. Turco Liveri, A. Longo. "Structural organization of the hydrophilic nanodomain of sodium bis(2-ethylhexyl) sulfosuccinate liquid crystals".

Meetings

- FIGIPAS 2009, Palermo 1-4 Luglio 2009, poster presentation;

- XAFS14 2009, Camerino 26 Luglio-1 Agosto 2009, poster presentation;

- SILS 2011 Trieste 1-3 Settembre 2011, oral presentation "HrXRD and EXAFS analysis of nanocristalline cobalt samples".

School

- XI School on Synchrotron Radiation: fundamentals, methods and applications Duino(Trieste), 5-16 September 2011;
- Giornate didattiche 2011 della SISN (Società italiana di spettroscopia neutronica) S.Giovanni(Bolzano) - Grenoble 25 June 2001-5 July 2011.

Experience

- Dates: October 2011
  AFM Experiment at ISMN-CNR (Bologna, Italy);
- Dates: April 2011
  AFM Experiment at ISMN-CNR (Bologna, Italy);
- Dates: 27 October-2 November 2010
  XAFS experiment at BM08 of ESRF (European Synchrotron Radiation Facility) Grenoble, France;
- Dates: 2-9 March 2010
  XAFS experiment at BM01 of ESRF (European Synchrotron Radiation Facility) Grenoble, France;
- Dates: 29 January – 02 February 2010
  SAXS and XAFS experiment at BM26 of ESRF (European Synchrotron Radiation Facility) Grenoble, France.

Attended courses

- Corso di Fisica della Materia. Prof. Aurelio Agliolo Gallitto.

Attended conferences

- "Materiali Molecolari Organici" Prof. Nazario Martín León;
- "Gold catalysis and its application" Prof. David Thompson;
- "Biosorption. Low cost sorbents for metal ions removal from aqueous solution" Prof. Isabel Villaescusa Gil;
- "NMR spectroscopy and chemometrics in food analysis" Prof. Apostolos Spyros;
- "Spin-off accademici nel settore dell R & S tecnologico" Dr. Giuseppe Currò;
- "Semiconduttori organici molecolari e polimerici fluorurati per la fotonica e l'elettronica" Prof. Gianluca Farinola;
- "Teoria e pratica di sistemi nanoparticellari in catalisi: nuove fasi metalliche ed ossidi superparamagnetici" Dott. Angelo Vargas;
- "Understanding reaction outcomes in ionic liquids – Can we achieve solvent-controlled reactivity?" Dr. Jason Harper;
- "Activated Peptides: for Ligation and Large Cyclic Transition States" Prof. Alan R. Katritzky
- "Giuseppe Oddo" Prof. Renato Noto;
- "Density Functional Simulations in Large Scale Systems with the SIESTA Method" Prof. Pablo Ordejòn.